Faculty of Science
Department of Physics
University of Helsinki

# ULTRASOUND IN CHARACTERIZATION OF ROCKS AND CERAMICS AND IN CRYSTALLIZATION CONTROL

**Ilkka Lassila**

ACADEMIC DISSERTATION

**Supervisor**
Professor Edward Hæggström
Department of Physics
University of Helsinki
Finland

**Reviewers**
Professor Yves Guéguen
Département de Géosciences
Ecole Normale Supérieure
France

Professor Jarno Salonen
Department of Physics and Astronomy
University of Turku
Finland

**Opponent**
Professor Emeritus David Greve
College of Engineering
Carnegie Mellon University
United States of America

# ABSTRACT

Deep continental drilling is a fundamental tool for obtaining detailed information about the composition, structure and physical conditions of the Earth's crust. A drill hole allows direct access to rock under *in situ* conditions and retrieval of core samples that can be investigated in laboratory. In order to get reliable estimates for geophysical properties of rock samples, the seismic velocity measurements should be performed under pressure. An apparatus was built that could be used to determine ultrasonic (1 MHz) longitudinal and shear wave velocities (*Vp* and *Vs)* in rock samples under uniaxial compression that resembles conditions in the crust down to 11 km depth. Rock samples from Outokumpu deep drill hole (2516 m) were analyzed to characterize the geophysical nature of the Precambrian crustal section in Eastern Finland. Velocities varied according to the mineral composition, lithology, porosity and microcracks. The core velocities increased with increasing pressure due to microcrack closure. The results agreed with the down-core direction velocities of samples from the same core section measured under triaxial compression using a multi-anvil apparatus to some extent.

The obtained geophysical parameters can be used to refine the interpretation of the seismic reflection survey data, such as the data from Finnish Reflection Experiment (FIRE) project. One of the FIRE survey lines crossed the Outokumpu area. The stress field in Fennoscandian crust consists of the weight of the overburden (26 MPa/km) and from a horizontal stress state arising from the Mid-Atlantic ridge push. The vertical stress exceeds the horizontal stresses at ~1 km depth. The crust exhibits velocity anisotropy that is strongly related to foliation and, in the case of retrieved core samples, to oriented microcracks. Because of seismic velocity anisotropy and the crustal stress-field, velocities should be measured in three dimensions under controlled tri-axial pressure, which is difficult with uniaxial apparatus. A multi-anvil apparatus was built to measure *Vp* and *Vs* (0° and 90° polarization) in three orthogonal directions of cube shaped samples under triaxial compression. Samples from the FIRE survey line were measured with the apparatus.

Ultrasonic velocity measurements were also used to determine the porosity of custom-made ceramic samples. At 4-33% porosity the velocity decreased linearly with increasing porosity for both *Vp* and *Vs.*

Material crystallinity is often a required property of the intermediate or end product in pharmaceutical manufacturing. Material can exhibit more than one crystal structure i.e. polymorph. While chemically identical the different lattice structure of an active pharmaceutical ingredient (API) results in different physicochemical properties. Polymorphism can significantly affect properties such as bioavailability, solubility and dissolution rate. These properties are also affected by the particle size, which is highlighted in case of nanoparticles.

Besides using ultrasound to measure material properties, ultrasound was used in semi-batch crystallizer to initiate nucleation and control polymorphism and size of *L-*

glutamic acid. Ultrasound-initiated nucleation produced pure (> 99.5 wt%) $\alpha$-polymorph in controlled supersaturation conditions and reduced the particle size.

# ACKNOWLEDGEMENTS

# CONTENTS

# LIST OF ORIGINAL PUBLICATIONS

I.    I. Lassila, R. Karlqvist, T. Elbra, F. K. Gates, L. J. Pesonen, and E. Hæggström, 'Ultrasonic velocity of the upper gneiss series rocks from the Outokumpu deep drill hole, Fennoscandian shield — Comparing uniaxial to triaxial loading', *Journal of Applied Geophysics*, vol. 72, no. 3, pp. 178–183, Nov. 2010.

II.   T. Elbra, R. Karlqvist, I. Lassila, E. Hæggström, and L. J. Pesonen, 'Laboratory measurements of the seismic velocities and other petrophysical properties of the Outokumpu deep drill core samples, eastern Finland', *Geophysical Journal International*, vol. 184, no. 1, pp. 405–415, 2011.

III.  T. Elbra, R. Karlqvist, I. Lassila, E. Hæggström, and L. Pesonen, 'P- and S-wave velocities of rocks from the upper 1.5 km crustal section sampled by the Outokumpu Deep Drilling Project, Finland.', *Outokumpu Deep Drilling Project 2003–2010*, 2011.

IV.   T. Kohout, R. Karlqvist, I. Lassila, J. Eskelinen, A. Hortling, L. J. Pesonen and E. Hæggström, 'Ultrasonic Determination of Porosity in Homogeneous Ceramic Samples', *Geophysica*, vol. 49, no. 1–2, pp. 25–32, 2013.

V.    H. Hatakka, H. Alatalo, M. Louhi-Kultanen, I. Lassila, and E. Hæggström, 'Closed-Loop Control of Reactive Crystallization PART II: Polymorphism Control of L-Glutamic Acid by Sonocrystallization and Seeding', *Chemical Engineering & Technology*, vol. 33, no. 5, pp. 751–756, May 2010.

# AUTHOR'S CONTRIBUTIONS

I.     I. Lassila (IL) Designed and assembled the measurement apparatus, performed the measurements and analyzed the data. He wrote the article manuscript which was refined together with all authors.

II.     IL wrote the ultrasonic instrumentation part of the manuscript and guided the measurements. He shared the responsibility of ultrasonic data analysis.

III.     IL wrote the ultrasonic instrumentation part of the manuscript and guided the measurements. He shared the responsibility of ultrasonic data analysis.

IV.     IL designed the experiments and refined the manuscript with all authors.

V.     IL performed preliminary testing and designed the ultrasonic experiments with all authors.

# ABBREVIATIONS

| | |
|---|---|
| API | Active pharmaceutical ingredient |
| ATR | Attenuated total reflection |
| BET | Brunauer, Emmett and Teller |
| CV | Coefficient of variation |
| EMT | Effective medium theory |
| EDX | Energy dispersive X-ray spectroscopy |
| FEM | Finite Element Method |
| FIRE | Finnish Reflection Experiment |
| FTIR | Fourier-transform infrared spectroscopy |
| GTK | Geological Survey of Finland |
| LVDT | Linear variable differential transformers |
| MSZW | Metastable zone width |
| NDT | Non-Destructive Testing |
| ODDP | Outokumpu Deep Drilling Project |
| PMMA | Polymethyl methacrylate |
| PSD | Particle-size distribution |
| SEM | Scanning electron microscopy |
| TEM | Transmission electron microscopy |
| *ToF* | Time of flight |
| *Vp* | Primary (longitudinal) wave velocity |
| *Vs* | Secondary (shear) wave velocity |

# 1. INTRODUCTION

## 1.1. The Earth's crust

The outer shell of the Earth is called the crust. It is 5-10 km thick under the oceans and grows towards the continents where it reaches 20-70 km. Oceanic and continental crust have different ages, compositions and properties. The crust can be distinguished from underlying parts of the Earth for example by its seismic velocities, densities, rock types, mineralogical and chemical descriptions. The outermost seismic discontinuity in the Earth is called the Mohorovicic discontinuity or Moho, which is the base of the crust above the mantle [1]–[3].

Knowledge of the crustal structure is important for understanding geological processes and evolutionary history [4]. It is also required in industrial applications such as mining [5]. Deep continental drilling is indispensable tool for obtaining information about the composition, structure and physical conditions in the crust [6]. A drill hole provides direct access to *in situ* conditions and it can be used in collecting bore hole samples [7]. The physical properties of the samples can then be measured in laboratory to constrain the geophysical models of the crust.

The Earth's physical properties can also be estimated using seismic waves. The waves, that can be man-made vibrations or earthquakes, travel in the Earth and reflect from rock interfaces. The depth of the reflecting structure can be interpreted from the travel times of the wave velocities. Determination of the velocity characteristics is a crucial task in the investigation of the Earth's crustal structure. The accuracy of the depth interpretations of the seismic observations depend on the accuracy of the velocity data [8]. The seismic velocities on the other hand depend on rock type and its mineralogical composition, porosity, microcrack density and prevailing physical conditions.

## 1.2. Outokumpu Deep Drilling

In the Outokumpu Deep Drill Project (ODDP) a 2516 m deep research bore hole R2500 with a 22 cm diameter was drilled in 2004-2005 in Outokumpu (Lat. 62.71740°N, Long. 29.06528°E), Eastern Finland, area well known for its metal ores that still indicates mining potential. The target Precambrian-aged (2,1-1,9 Ga) rocks consist of mica schists, biotite gneiss, chlorite-sericite schist, black schist, serpentinites, diopside, tremolite skarns and pegmatite granites. The project that took place in 2003-2010 was coordinated by Geological Survey of Finland (GTK) and was carried out in an international framework. One of the main tasks of the project was to reveal the geological nature of strong seismic reflectors (2-2,5 km depth) and explore the mining potential. The regionally exceptional drilling depth enabled scientific possibilities to unveil the deep structure of the ore belt. The drilling produced drill core samples throughout the hole with a final core recovery of 79% [7]. The ODDP core samples formed the main sample set in this dissertation.

## 1.3. FIRE: Finnish Reflection Experiment

Finnish Reflection Experiment (FIRE) project was carried out across Finland in 2001-2005. It investigated the structure and evolution of the Earth's crust using reflection seismic surveys. Seismic waves were created by five 15.4-ton vibrator trucks that applied linear-frequency sweeps from 12 to 80 Hz with a force of 10 ton/vibrator. The signal length was 30 s and the recording time 60 s. The source interval was 100 m. The signal was acquired using 362 geophone groups at 50 m intervals. The survey lines with total length of 2104 km crossed all major geological units in Finland (Figure 1). One of the profiles (FIRE3) crossed the Outokumpu ore belt and made possible to compare high-resolution seismic data with the drilling results [9]. Ultrasonic velocities of surface rock samples from the FIRE-reflection profile were measured in this study.
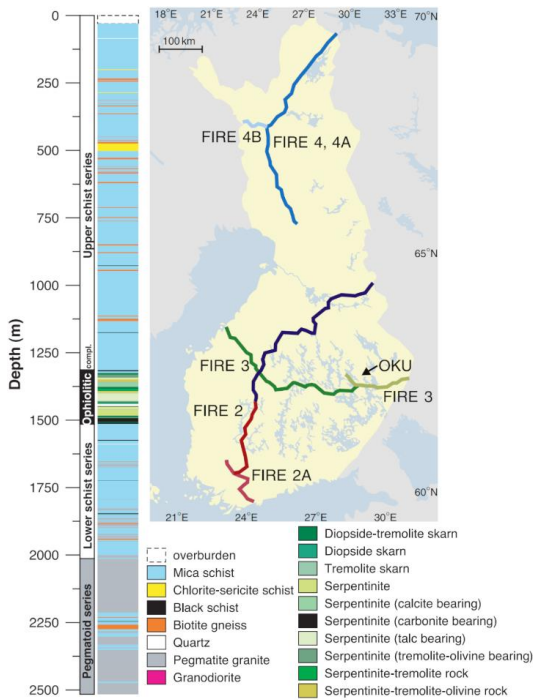


Figure 1. Lithology of the Outokumpu deep drill core and FIRE seismic survey transect lines. The Upper schist series (33-1314 m) consists mainly of mica schists with some biotite gneiss, chlorite-sericite schist and black schist intercalations. It is followed by the ophiolitic complex (1314-1515 m) consisting of serpentinites, diopside and tremolite skarns and black schists. Lower schist series (1515-2013 m) consist of mica schist, biotite gneiss and chlorite-sericite schists as well as black schists. Pegmatoid series (2013-2516 m) include pegmatite granites with layers of biotite gneiss. The four FIRE reflection seismic transects are selected based on geological relevance, previous wide-angle reflection/refraction data and availability of roads   [7], [9], [9], [10].

## 1.4. Porosity and microcracks

Porosity is a measure of the void spaces in a material ranging from 0 to 100%. It is an important structural feature in natural and man-made materials and often affects

significantly physical properties such as fluid permeability, thermal conductivity, electrical conductivity, dielectric constant, magnetic permeability, diffusion coefficient, acoustic wave velocities, elastic moduli, and yield, rupture or ductile strength [11]. Typical porosities in rock are 5-30% [12]. In geology porosity has an important role in fluid flow and storage [13]. In rocks the porosity varies usually with the mineral composition. Porosity effect on sound velocities was studied using ceramic samples. Ceramics of different porosity but similar mineral composition were manufactured by adjusting the firing temperature. Ceramic materials are hard and have high resistance to abrasion, corrosion and thermal shocks. Hence they are often used in thermomechanical applications [14].

Microfractures or microcracks are high-aspect ratio cracks in rock whose length is generally less than 100 μm. These cracks can be lens or tabular shaped. The rock properties, such as strength and permeability, can be largely governed by the microcracks [15]. Microcracks are formed when the local stress exceeds the local strength. Spatial and temporal temperature variations can also induce cracking. Application of hydrostatic pressure in the range of 100 – 200 MPa closes most cracks, but the closure is affected by the crack surface roughness [16].

## 1.5. Crystallization

Material is considered crystalline if its constituents (atoms, ions or molecules) are arranged with long-range order [17]. Crystallization from solution is a phase change in which a crystalline material is obtained from a solution.

Reactive crystallization is a process where supersaturation is created through chemical reaction. In reactive crystallizations the high level of supersaturation results in high nucleation rates and small crystal size. The process is widely used in chemical and pharmaceutical industry to make intermediates and finished products [18], [19].

In sonocrystallization ultrasound is applied to solution to affect crystallization. It can have a significant effect on the produced crystal [18]. High intensity ultrasound in solution generates cavitation that results in enhanced micromixing, increased mass transfer rate, reduces metastable zone width, increases nucleation rate and narrows down particle size and size distribution [20]. The production of specific particle size and polymorph is often required. This is critical for example in pharmaceutical industry as the particle size and polymorph dictate the product quality and effectiveness [21].

## 1.6. Aims

The aim of this thesis was to use ultrasound to characterize material and control crystallization. A device was built to measure *Vp* and *Vs* of rock core samples in crustal conditions under uniaxial loading. In Paper I the results obtained with the device were compared to results measured with multi-anvil device. The constructed device was

used to measure drill core samples from ODDP which was described in Paper II and Paper III along with the physical interpretation of the results. Seismic velocity measurements were extended to velocity anisotropy measurements for which a new device was built. This was described in the supporting conference article [22]. A relation between porosity and ultrasonic velocities of ceramic samples was indicated in paper IV. Besides using ultrasound for measuring material properties it was also used to initiate crystallization and control the produced polymorph of crystals and particle size. This was described in Paper V.

Claim: Ultrasound can be used to monitor mechanical properties of rock samples from R2500 deep drill core and FIRE survey lines using custom ultrasonic apparatus, and to induce crystallization of $L$-glutamic acid and control its polymorph and particle size.

# 2. THEORY AND BACKGROUND

## 2.1. Ultrasound propagation

Sound is mechanical energy, a vibration or wave-field that propagates through medium. It is in many ways analogous to electromagnetic wave such as light. The frequency of seismic waves can be less than 1 Hz whereas waves with frequencies above human audible region (20 kHz) are called ultrasound [23].

Possible elastodynamic wave modes that can propagate in media depend on the material properties and boundary conditions. Gas and liquid can support longitudinal wave mode. Solid material supports also shear wave propagation. A wave can travel on surfaces via Rayleigh mode, in plates via Lamb and Love waves, at solid-solid interface via Stoneley waves and at solid-liquid interface via Scholte waves. Also, more specific wave modes can be found for different geometries such as rods and hollow cylinders [24], [25]. The modes of interest in this thesis are the longitudinal and shear wave, which in geophysics are called $P$- and $S$-waves (primary and secondary or shear wave respectively) [26]. The particle motion in the longitudinal wave is in the direction of the wave propagation and in shear wave perpendicular to it. In general, waves propagating in solid medium may combine longitudinal and shear motion.

Propagation of mechanical wave is governed by Newton's law

$$\boldsymbol{F} = m\boldsymbol{a} \tag{1}$$

and Hooke's law

$$\boldsymbol{F} = k\boldsymbol{x}, \tag{2}$$

where $\boldsymbol{F}$ is force, m is mass, k is spring constant and $\boldsymbol{x}$ is displacement. Wave equation in three dimensions is described by

$$\nabla^2 \varphi = \frac{1}{c^2} \frac{\partial^2 \varphi}{\partial t^2}, \tag{3}$$

13

where $\varphi$ is field variable, $c$ is wave velocity, and $t$ is time. The plane wave solution to this equation is

$$\varphi = Ae^{-i(\mathbf{k}\cdot\mathbf{x}-\omega t)}, \tag{4}$$

where $A$ is amplitude $\mathbf{k}$ is wave vector, $\mathbf{x}$ is position vector and $\omega$ is angular frequency.

The stress $\sigma$ and strain $e$ have linear relationship

$$\sigma_{ij} = c_{ijkl}e_{kl}, \tag{5}$$

where $c$ is elastic parameter tensor or the stiffness tensor. This empirical equation is valid for small deformations acting for short times [26]. If strain is represented as a function of stress, the relationship is

$$e_{ij} = s_{ijkl}\sigma_{kl}, \tag{6}$$

where $s$ is the elastic compliance tensor. For an isotropic material, the number of independent constants reduces to two and the tensor of elasticity becomes

$$\begin{bmatrix} c_{11} & c_{12} & c_{12} & 0 & 0 & 0 \\ c_{12} & c_{11} & c_{12} & 0 & 0 & 0 \\ c_{12} & c_{12} & c_{11} & 0 & 0 & 0 \\ 0 & 0 & 0 & c_{44} & 0 & 0 \\ 0 & 0 & 0 & 0 & c_{44} & 0 \\ 0 & 0 & 0 & 0 & 0 & c_{44} \end{bmatrix}, \tag{7}$$

with $c_{12}=c_{11}-2c_{44}$. The relationship between the components and the Lamé parameters $\lambda$ and $\mu$ (shear modulus) are

$$c_{11} = \lambda + 2\mu, c_{12} = \lambda, c_{44} = \mu. \tag{8}$$

Furthermore, in homogeneous linear elastic material the elastic properties are uniquely determined by any two moduli (Bulk modulus $K$, Young's modulus $E$, Lame's first parameter $\lambda$, Shear modulus $\mu$, Poisson's ratio $v$ and longitudinal modulus $M$) and the remaining four moduli can be calculated using them (Appendix A) [27].

The acoustic wave velocities in homogenous, isotropic, elastic media are:

$$V_p = \sqrt{\frac{K + \frac{4}{3}\mu}{\rho}} = \sqrt{\frac{\lambda + 2\mu}{\rho}} \tag{9}$$

$$V_s = \sqrt{\frac{\mu}{\rho}} \tag{10}$$

$$V_e = \sqrt{\frac{E}{\rho}}, \tag{11}$$

where $Vp$ and $Vs$ are the P- and S-wave velocities and $Ve$ is the extensional velocity in a narrow bar.

14

The elastic moduli can be extracted from density ($\rho$) and the wave velocities.

$$M = \rho V_p^2 \tag{12}$$

$$E = \rho V_e^2 \tag{13}$$

$$\mu = \rho V_s^2 \tag{14}$$

$$\lambda = \rho(V_p^2 - 2V_s^2) \tag{15}$$

$$K = \rho\left(V_p^2 - \frac{4}{3}V_s^2\right) \tag{16}$$

$$\nu = \frac{V_p^2 - 2V_s^2}{2\left(V_p^2 - V_s^2\right)} \tag{17}$$

[28], [29]. The moduli represent the material stress strain relations.

In ultrasonic velocity measurements of rock samples, the velocity determined by the first arrival does not always correspond to an easily identified velocity. The ultrasonic waves in rocks are seldom monochromatic, but instead they have a finite bandwidth. The wave can be considered as a superposition of monochromatic waves with different frequencies, which gives rise to the concept of wave groups. These wave groups or the modulation on a wave containing a band of frequencies, propagate with a group velocity, which can be expressed as

$$V_{group} = V_{phase} - \lambda \frac{dV_{phase}}{d\lambda}, \tag{18}$$

$$V_{group} = V_{phase} + k \frac{dV_{phase}}{dk} \text{ or} \tag{19}$$

$$\frac{1}{V_{group}} = \frac{1}{V_{phase}} - \frac{\omega}{V_{phase}^2}\frac{dV_{phase}}{d\omega}, \tag{20}$$

where $\lambda$ is the wavelength, $k$ is wave vector and $\omega$ angular frequency. This shows that if the phase velocity is frequency dependent, direction dependent or both, the group velocity is different from phase velocity. Dispersion is called *normal* if the group velocity decreases with frequency, such as propagation in wave guide, and *anomalous* if it increases with frequency, such as propagation in homogeneous viscoelastic medium (intrinsic dissipation). For a non-dispersive wave, the group and phase velocities coincide.

## 2.2. Reflection and refraction

The specific acoustic impedance is the ratio of acoustic pressure $p$ to the associated particle speed $u$ at that point

$$Z = \frac{p}{u}, \tag{21}$$

which for plane waves is

$$Z = \pm\rho c,\tag{22}$$

where $\rho$ is density of the material and $c$ sound velocity in it. When a plane wave encounters an interface of two materials, it is divided into components. Some energy is transmitted and some reflected. The components of the displacement vectors are continuous across the interface. The reflection $R$ and transmission $T$ coefficients for a wave propagating from material with $Z_1$ to $Z_2$ are

$$R = \frac{Z_2 - Z_1}{Z_1 + Z_2},\tag{23}$$

and

$$T = \frac{2Z_2}{Z_1 + Z_2}.\tag{24}$$

At non-normal incidence, the incident $P$-wave generates reflected $P$- and $S$-waves and transmitted $P$- and $S$-waves. The angles of the reflected and refracted waves are determined by the Snell's law

$$p = \frac{\sin\theta_1}{V_{P1}} = \frac{\sin\theta_2}{V_{P2}} = \frac{\sin\theta_{S1}}{V_{S1}} = \frac{\sin\theta_{S2}}{V_{S2}},\tag{25}$$

while the amplitudes for them are given by Zoeppritz equations [25], [29]–[34].

## 2.3. Velocity dispersion

The stress-strain relation of viscoelastic material is time-dependent [29]. The displacement for a wave propagating in a viscoelastic material is given by

$$u(x,t) = u_0 e^{-\alpha(\omega)x} A e^{-i(\mathbf{k}\cdot\mathbf{x}-\omega t)},\tag{26}$$

then the stress and strain are out of phase

$$\sigma = \sigma_0 e^{i(\omega t - kx)},\tag{27}$$

$$e = e_0 e^{i(\omega t - kx - \alpha)}.\tag{28}$$

The main source of velocity dispersion in rock is presence of fluids along with porosity, texture and stress [35]–[37]. Dispersion can also occur with wave guides. The analytical solutions for the dispersion curves of waves propagating in solid rod can be obtained with Pochhammer–Chree equation. In a cylindrical rod the phenomenon appears when the radius $a$ of the rod is comparable to the wavelength $\lambda$ [38]. With very small ratio of $a/\lambda$ the measured velocity approximates the Young's modulus velocity $V_E$, with $a/\lambda$ approaching unity, the velocity approaches Rayleigh surface wave velocity and with large values of $a/\lambda$ the measured velocity approaches the bulk velocity $V_p$ [39]. In the case of 12.5 mm radius rock samples and ~3-5 mm wavelength the geometrical dispersion was considered small.

## 2.4. Effective elastic properties of rocks with cracks

Rocks are inherently heterogenous. They constitute from multiple components, such as different mineral grains and pore spaces. Although cracks in rock represent a small amount of porosity, they play a major role in elastic properties of the rocks in the upper crust [40]–[46]. In upper crustal conditions the pressure is inadequate to close the cracks [36]. The theories of effective elastic properties predict that microcracking causes degradation of stiffness, development of anisotropy and changes in wave speeds [47].

The micro cracks in rock can be divided into grain boundary cracks (associated with grain boundaries), intragranular cracks (within a grain), intergranular cracks (along the boundaries of two or more grains) and transgranular cracks (running across the grains) [16]. To understand the relation between the small-scale components and the measured bulk properties a simplification must be done. Several models for predicting material properties as a function of damage have been developed in the framework of Effective Medium Theories (EMT).

To predict the effective elastic moduli of a rock consisting of grains and pores, the volume fractions of the different phases, their elastic moduli, and geometric details need to be specified. With only the volume fractions and the constituent moduli we can predict the upper and lower bounds of the effective modulus. The precise value resides between the bounds depending on the geometric details [29]. The simplest estimates of the effective elastic modulus are the Voigt [48] and Reuss [49] estimates. Hill [50] demonstrated that these estimates were the upper and lower bounds. The Voigt upper bound $M_V$ of $N$ phases is

$$M_V = \sum_{i=1}^{N} f_i M_i,$$

(29)

where $f_i$ is the volume fraction of the $i$th phase and $M_i$ is the corresponding elastic modulus. The Voigt bound gives the ratio of average stress to average strain when all constituents are assumed to have the same strain.

The Reuss lower bound $M_R$ is

$$\frac{1}{M_R} = \sum_{i=1}^{N} \frac{f_i}{M_i}.$$

(30)

The Reuss bound gives the ratio of average stress to average strain when all constituents are assumed to have the same stress. A common estimate for the effective moduli is the average of the Voigt and Reuss bounds, referred as the Voigt-Reuss-Hill average, which can provide accurate estimate for isotropic rock.

An alternative Hashin–Shtrikman technique fills the space with concentric spheres without specifying the geometries of the constituents [51]. For material with two constituents, the bounds are

$$K^{\text{HS}\pm} = K_1 + \frac{f_2}{(K_2 - K_1)^{-1} + f_1 \left(K_1 + \frac{4}{3}\mu_1\right)^{-1}} \tag{31}$$

$$\mu^{\text{HS}\pm} = \mu_1 + \frac{f_2}{(\mu_2 - \mu_1)^{-1} + 2f_1(K_1 + 2\mu_1)/[5\mu_1\left(K_1 + \frac{4}{3}\mu_1\right)]}, \tag{32}$$

where $K_1$ and $K_2$ are the bulk moduli, $\mu_1$ and $\mu_2$ the shear moduli, and $f_1$ and $f_2$ the volume fractions of the individual phases. The expressions yield the upper bound when the stiffest material is termed 1 while the lower bound is obtained when the softest material is termed 1.

The simplest approximation scheme for cracked solids is the non-interacting crack approximation by Bristow [52]. The effective moduli can be found exactly for isotropic material for an arbitrary crack orientation statistic using the non-interaction approximation. Each crack is considered as an isolated one, embedded into the externally applied stress field and does not experience influence of other cracks.

A model for the effective moduli of cracked, transversely isotropic material is given by Cheng[29], [53]. It is based on static solution for the strain inside an ellipsoidal inclusion in an isotropic matrix. The effective moduli $c_{ij}^{\text{eff}}$ for a rock with fluid filled ellipsoidal cracks with their normals aligned along the 3-axis are given as

$$c_{ij}^{\text{eff}} = c_{ij}^0 - \varphi c_{ij}^1, \tag{33}$$

where $\varphi$ is the porosity and $c_{ij}^0$ are the moduli of uncracked isotropic rock. The corrections $c_{ij}^1$ are

$$c_{11}^1 = \lambda(S_{31} - S_{33} + 1) + \frac{2\mu E}{D(S_{12} - S_{11} + 1)} \tag{34}$$

$$c_{33}^1 = \frac{(\lambda + 2\mu)(-S_{12} - S_{11} + 1) + 2\lambda S_{13} + 4\mu C}{D} \tag{35}$$

$$c_{13}^1 = \frac{(\lambda + 2\mu)(S_{13} + S_{31}) - 4\mu C + \lambda(S_{13} - S_{12} - S_{11} - S_{33} + 2)}{2D} \tag{36}$$

$$c_{44}^1 = \frac{\mu}{1 - 2S_{1313}} \quad c_{66}^1 = \frac{\mu}{1 - 2S_{1212}} \tag{37}$$

$$c_{66}^1 = \frac{\mu}{1 - 2S_{1212}}, \tag{38}$$

where

$$C = \frac{K_{\text{fl}}}{3(K - K_{\text{fl}})} \tag{39}$$

$$D = S_{33}S_{11} + S_{33}S_{12} - 2S_{31}S_{13} - (S_{11} + S_{12} + S_{33} - 1 - 3C) \tag{40}$$
$$- C[(S_{11} + S_{12} + 2(S_{33} - S_{13} - S_{31})]$$

$$E = S_{33}S_{11} - S_{31}S_{13} - (S_{33} + S_{11} - 2C - 1) + C(S_{31} + S_{13} - S_{11} - S_{33}) \tag{41}$$

$$S_{11} = QI_{aa} + RI_a \quad S_{33} = Q\left(\frac{4\pi}{3} - 2I_{ac}\alpha^2\right) + I_c R \tag{42}$$

18

$$S_{12} = QI_{ab} - RI_a \quad S_{13} = QI_{ac}\alpha^2 - RI_a \tag{43}$$

$$S_{31} = QI_{ac} - RI_c \quad S_{1212} = QI_{ab} + RI_a \tag{44}$$

$$S_{1313} = \frac{Q(1 + \alpha^2)I_{ac}}{2} + \frac{R(I_a + I_c)}{2} \tag{45}$$

$$I_a = \frac{2\pi\alpha(\cos^{-1}\alpha - \alpha S_a)}{S_a^3} \quad I_c = 4\pi - 2I_a \tag{46}$$

$$I_{ac} = \frac{I_c - I_a}{3S_a^2} \quad I_{aa} = \pi - \frac{3I_{ac}}{4} \quad I_{ab} = \frac{I_{aa}}{3} \tag{47}$$

$$\sigma = \frac{3K - 2\mu}{6K + 2\mu} \quad S_a = \sqrt{1 - \alpha^2} \tag{48}$$

$$R = \frac{1 - 2\sigma}{8\pi(1 - \sigma)} \quad Q = \frac{3R}{1 - 2\sigma} \tag{49}$$

In the previous equations, $K$ and $\mu$ are the bulk and shear moduli of the isotropic matrix, respectively. $K_{\mathrm{fl}}$ is the bulk modulus of the fluid and $\alpha$ is the crack aspect ratio. Dry cavities are modelled by setting the inclusion moduli to zero. With fluid saturated cavities, the inclusion shear modulus is set to zero. The model is valid for arbitrary aspect ratios and is used to obtain the effective anisotropic stiffness tensor for transversely isotropic, cracked rocks. The model assumes isotropic, homogenous, elastic background matrix and an idealized ellipsoidal crack shape. It is limited to low crack concentration but can handle all crack aspect ratios. Because the cavities are isolated with respect to flow, the approach resembles high frequency behavior, such as ultrasonic laboratory measurements [29].

## 2.5. Rock anisotropy

In simplified characterization, rock is frequently treated as isotropic medium, with identical properties in all directions. However, most sedimentary, and metamorphic rocks are anisotropic thus significant errors can be introduced in the mechanical analyses by assuming isotropy. While multiple mechanisms may contribute to anisotropy, such as crystal alignment, grain alignment, stress-induced alignment of cracks, and thin sedimentary beds, seismic anisotropy is a common phenomenon for fractured rocks in the earth crust. Anisotropy is commonly found with sedimentary rocks that have different elastic properties in and perpendicular to the bedding planes, or metamorphic rocks such as slates that have a well-defined plane of cleavage. The anisotropy is not limited to laminated and layered rocks [32], [54], [55].

Anisotropic rock has more than two independent elastic coefficients. Because both stress and strain are second-order tensors with nine components, the most general linear stress-strain relationship can be expressed with a fourth-order tensor that has 81 components. As some of the components are interdependent, 36 components are required for the general version of Hooke's law. In Voigt notation the stress strain relationship is written as

$$\begin{bmatrix} \sigma_{xx} \\ \sigma_{yy} \\ \sigma_{zz} \\ \sigma_{yz} \\ \sigma_{xz} \\ \sigma_{xy} \end{bmatrix} = \begin{bmatrix} c_{11} c_{12} c_{13} c_{14} c_{15} c_{16} \\ c_{21} c_{22} c_{23} c_{24} c_{25} c_{26} \\ c_{31} c_{32} c_{33} c_{34} c_{35} c_{36} \\ c_{41} c_{42} c_{43} c_{44} c_{45} c_{46} \\ c_{51} c_{52} c_{53} c_{54} c_{55} c_{56} \\ c_{61} c_{62} c_{63} c_{64} c_{65} c_{66} \end{bmatrix} \begin{bmatrix} \varepsilon_{xx} \\ \varepsilon_{yy} \\ \varepsilon_{zz} \\ 2\varepsilon_{yz} \\ 2\varepsilon_{xz} \\ 2\varepsilon_{xy} \end{bmatrix}. \tag{50}$$

The matrix is always symmetric, so at most 21 of the components can be independent and the Hooke's law can be written as

$$\begin{bmatrix} \sigma_{xx} \\ \sigma_{yy} \\ \sigma_{zz} \\ \sigma_{yz} \\ \sigma_{xz} \\ \sigma_{xy} \end{bmatrix} = \begin{bmatrix} c_{11} c_{12} c_{13} c_{14} c_{15} c_{16} \\ c_{21} c_{22} c_{23} c_{24} c_{25} c_{26} \\ c_{13} c_{23} c_{33} c_{34} c_{35} c_{36} \\ c_{14} c_{24} c_{34} c_{44} c_{45} c_{46} \\ c_{15} c_{25} c_{35} c_{45} c_{55} c_{56} \\ c_{16} c_{26} c_{36} c_{46} c_{56} c_{66} \end{bmatrix} \begin{bmatrix} \varepsilon_{xx} \\ \varepsilon_{yy} \\ \varepsilon_{zz} \\ 2\varepsilon_{yz} \\ 2\varepsilon_{xz} \\ 2\varepsilon_{xy} \end{bmatrix}. \tag{51}$$

Triclinic crystals fall into this category. If material exhibits physical symmetry, the number of independent stiffnesses can be further reduced. The Voigt elastic stiffness matrix for monoclinic medium orthogonal to the $x_3$-axis has 13 independent constants:

$$\begin{bmatrix} c_{11} c_{12} c_{13} & 0 & c_{15} & 0 \\ c_{21} c_{22} c_{23} & 0 & c_{25} & 0 \\ c_{13} c_{23} c_{33} & 0 & c_{35} & 0 \\ 0 & 0 & 0 & c_{44} & 0 & c_{46} \\ c_{15} c_{25} c_{35} c_{45} c_{55} & 0 \\ 0 & 0 & 0 & c_{46} & 0 & c_{66} \end{bmatrix}. \tag{52}$$

The Voigt elastic stiffness matrix for orthorombic material when each Cartesian coordinate plane is aligned with a symmetry plane of the material has 9 independent constants:

$$\begin{bmatrix} c_{11} c_{12} c_{13} & 0 & 0 & 0 \\ c_{12} c_{22} c_{23} & 0 & 0 & 0 \\ c_{13} c_{23} c_{33} & 0 & 0 & 0 \\ 0 & 0 & 0 & c_{44} & 0 & 0 \\ 0 & 0 & 0 & 0 & c_{55} & 0 \\ 0 & 0 & 0 & 0 & 0 & c_{66} \end{bmatrix}. \tag{53}$$

Similarly aligned hexagonal or transversely isotropic material has 5 independent constants:

$$\begin{bmatrix} c_{11} c_{12} c_{13} & 0 & 0 & 0 \\ c_{12} c_{11} c_{13} & 0 & 0 & 0 \\ c_{13} c_{13} c_{33} & 0 & 0 & 0 \\ 0 & 0 & 0 & c_{44} & 0 & 0 \\ 0 & 0 & 0 & 0 & c_{44} & 0 \\ 0 & 0 & 0 & 0 & 0 & c_{66} \end{bmatrix}, c_{66} = \frac{1}{2}(c_{11} - c_{12}) \tag{54}$$

and cubic material 3 independent constants:

$$\begin{bmatrix} c_{11} & c_{12} & c_{12} & 0 & 0 & 0 \\ c_{12} & c_{11} & c_{12} & 0 & 0 & 0 \\ c_{12} & c_{12} & c_{11} & 0 & 0 & 0 \\ 0 & 0 & 0 & c_{44} & 0 & 0 \\ 0 & 0 & 0 & 0 & c_{44} & 0 \\ 0 & 0 & 0 & 0 & 0 & c_{44} \end{bmatrix}. \tag{55}$$

In situations, where the symmetry axes of the rock are in an oblique angle to the measurement direction, the stress-strain equations take on a more complicated form, that can be found by transforming both stresses and strains into the new coordinate system using transformation laws [29], [32].

## 2.6. Pressure and temperature effects on velocities

Pressure and temperature affect the elastic wave velocities usually in opposite manner. The effects vary between different rock types. As the pressure is increased, the cracks and pores are closed and contacts between the rock forming minerals are improved and stiffened. In the low-pressure range, the rise of velocities is rapid and nonlinear. The near complete closing of cracks is indicated by the transition to a linear velocity increase that represents the intrinsic velocities of the compacted aggregate [33], [56]–[60]. The closing of cracks in fluid saturated rock is determined by the differential stress, that is the difference between the stress imposed on the rock and the liquid pressure. The increase of velocity with increase in confining pressure can be cancelled out by an increase in pore pressure [61]–[63].

In many cases, the temperature affects the velocities in an opposite way than pressure. Thermal expansion loosens the structure, opens new cracks, and widens old cracks which decreases the elastic wave velocities. The contact conditions can change also due to different thermal expansion properties of rock-forming minerals. The temperature induced velocity decrease is highly dependent on the pressure exerted on rock. The velocity decrease is often non-linear at low confining pressure, while tending to be more linear at higher pressure. Sufficient pressure can prevent thermal cracking. In such case, increasing temperature can reduce pore volume, which can lead also to velocity increase. Temperature can affect the elasticity of both the rock forming minerals and the pore constituents [58], [59], [64]–[66].

## 2.7. Porosity measurement techniques suitable for rocks

Rock or ceramic porosity can be directly measured using several fluid based techniques, such as: saturation (using e.g., synthetic brine or toluene), buoyancy, gas expansion (notably helium porosimetry), gas adsorption (specific surface area determined by BET) and mercury intrusion capillary pressure. These are only sensitive

to interconnected pores. Imaging methods that have been used include optical light microscopy, scanning electron microscopy (SEM), energy dispersive X-ray spectroscopy (EDX), focused ion beam SEM, transmission electron microscopy (TEM), nuclear magnetic resonance imaging and X-ray and neutron tomography. Also, thermoporometry, ultrasonic velocity and attenuation, muon spin resonance, positron annihilation spectroscopy have been used to assess porosity [13], [67], [68]. Also destructive testing has been used, such as C-14-PMMA impregmentation method [69].

## 2.8. Porosity and pore saturation

Porosity affects significantly acoustic wave propagation in porous material [70]. Generally velocity decreases with increasing porosity [71]. This applies also to both *Vp* and *Vs* [72].

Various theories for wave propagation in saturated porous material have been proposed. One of the most influential is Biot theory [73], [74], which describes elastic wave propagation through fully fluid saturated solid matrix. The hydrodynamic interaction between the fluid and matrix is separated into inertia interaction and viscous interaction. Biot's theory is used for estimating frequency-dependent saturated-rock velocities from dry-rock velocities. The assumptions and limitations for using Biot's theory are that the rock is isotropic, all minerals in rock have the same bulk and shear moduli, the fluid-bearing rock is completely saturated, the pore fluid is Newtonian, and the wavelength is much larger than the grain or pore scale [29].

The Gassman's equations [75] are widely used relations to calculate the effect of pore-fluid saturation to seismic velocities. The bulk modulus is given by

$$K_{sat} = K_{dry} + \frac{\left(1 - \frac{K_{frame}}{K_s}\right)^2}{\frac{\varphi}{K_{fl}} + \frac{1-\varphi}{K_s} - \frac{K_{dry}}{K_s^2}},$$

(56)

Where $K_{sat}$, $K_{dry}$, $K_s$, and $K_{fl}$ are the bulk moduli of the saturated rock, dry porous rock frame, solid rock component, and pore fluid, respectively and $\varphi$ is the porosity. The velocities are

$$V_p = \sqrt{\frac{k_{dry} + \frac{\left(1 - \frac{k_{dry}}{k_s}\right)^2}{\frac{\varphi}{k_{fl}} + \frac{1-\varphi}{k_s} - \frac{k_{dry}}{k_s^2}} + \frac{4}{3}\mu_{dry}}{(1-\varphi)\rho + \varphi\rho_{fl}}}$$

(57)

and

$$V_s = \sqrt{\frac{\mu_{dry}}{(1-\varphi)\rho_s + \varphi\rho_{fl}}},$$

(58)

where $\mu_{dry}$, $\rho_s$ and $\rho_{fl}$ are the shear modulus of the dry rock, densities of the solid rock component and pore fluid, respectively [33].

As elastic waves propagate in porous media, the pore filling fluid influences the waves: (1) There is an influence for the whole rock-fluid system with the increased density and effective stiffening when pore gas is changed to liquid, (2) the fluid can affect the inter particle contact conditions and "soften the matrix", (3) in a multiphase system (e.g. brine and air) stress components arise from interfacial tension and capillary forces.

Typically, the velocity increases similarly with increasing pressure regardless of the saturation. Compressional wave velocity increases corresponding to the wave velocity in the fluid. With shear wave, if the rock skeleton is not softened by the saturation, there is no influence on the shear modulus, but the density change affects the wave velocity. In case of partial saturation, the pore size distribution and capillary pressure determine how the saturation increases the velocity. Gas is compressible and with total water saturation the compression modulus reaches higher value. The shear modulus is less effected by the pore filling because the shear modulus of liquid is zero. Small decrease of shear wave velocity typically rises from increase of density with increasing water saturation [27].

The ratio of $Vp/Vs$ is often calculated from the measured velocity data because it is more sensitive to the saturating fluid type and to crack, or pore, geometry, than $Vp$ or $Vs$ alone. High $Vp/Vs$ ratios and low velocities may also arise from strong mineral preferred orientation [76].

## 2.9. Velocity measurement configurations

Three measurement configurations are commonly used for determination of elastic wave velocities: (1) Measurement along the axis of a cylindrical sample with axial loading and (2) measurement in three directions with cube-shaped samples in a multi-anvil apparatus. This configuration can be used to measure velocity anisotropy with a single sample. Determination of velocity anisotropy with cylindrical samples requires three separate samples that are prepared along orthogonal directions [77]. (3) Measuring under hydrostatic pressure using water, oil or nitrogen as confining pressure medium [78]–[80]. Elastic anisotropy can be determined from velocities measured in multiple directions with spherical rock samples under hydrostatic pressure [81].

Multi-anvil is a device that can be used to apply high pressure along more than one axis of loading and four or more anvils compressing sample [82]. It is also referred to as true-triaxial pressure apparatus. The terms triaxial and multi-anvil terms are also used synonymously [83].

Triaxial loading typically refers to configuration where the sample is loaded in one (vertical) direction and a fluid pressure is applied to the lateral surface.

Ultrasonic testing is widely used for nondestructive testing (NDT) of rocks. As elastic wave propagates in material the wave interacts with it. The material's physical

properties and microstructural characteristics, such as crystal and void size and shape distribution, determine the velocities, and amplitude-frequency spectra of the elastic wave. While the seismic soundings rely on the reflections from the seismic impedance contrasts and pulse-echo or pitch-catch methods are used, the recommended method for laboratory measurement of rocks is to use through transmission, pitch catch method. This is because the direction and length of the signal path is known with higher confidence in direct-transmission configuration. Also the sample surface and edge properties influence less the measurement [84].

## 2.10. Crustal conditions

The lithostatic pressure increases with depth and is a function of rock density. The vertical stress is predictable from the weight of the overburden. The gravitational loading causes vertically aligned stress of magnitude $S_v = \rho g H$, where $\rho$ is the density of the overlying crust, $g$ acceleration of gravity and $H$ the depth [85] (Figure 2). For an average density of 2700 kg/m³ [7], the pressure increase with depth is 26 MPa/km.
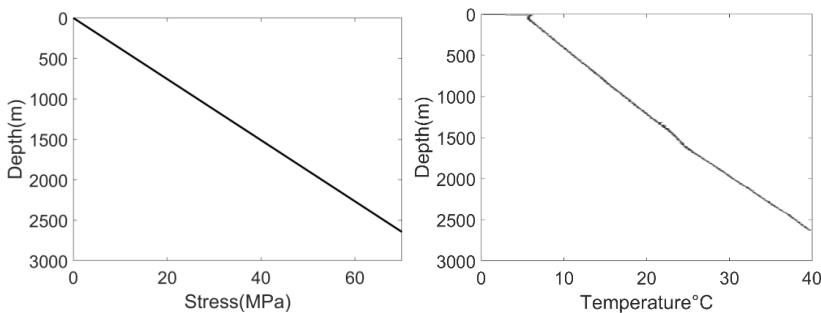


Figure 2. Left: The vertical component of lithostatic pressure increases 26 MPa/km, corresponding for average density of overburden of 2700 kg/m³. Right: Temperature of the Outokumpu Deep Drill Hole (measured on 5th of September 2008). Adapted from [86].

The uppermost 1000 m of Fennoscandian bedrock encounters large horizontal stress component that exceeds the vertical stress estimated from the weight of the overburden. The stress state arises from the ridge push from the Mid-Atlantic Ridge combined with the repercussion from the last ice age [87], [88]. A detailed estimation of the stressed state of the rock mass in Outokumpu can be found in literature [89].

The geothermal properties of the Outokumpu hole have been thoroughly studied. The most important factors affecting the subsurface temperatures are the thermal conductivity structure and past climatic variations in ground surface temperature, especially glaciations [90]. The post-drilling logs reveal temperature gradient with a vertical increase in temperature from $13 - 14$ mK m$^{-1}$ at 50 m $- 1.3$ km, $10 - 13$ mK m$^{-1}$ at 1.3 km $- 1.5$ km, 16 mK m$^{-1}$ at $1.5 - 2.2$ km and 13 - 16 mK m$^{-1}$ at $2.2 - 2.5$ km. At the final 2.5 km depth the temperature reaches nearly 40°C [86].

## 2.11.  Basic methods of micro-structure observation in rock samples

Different minerals in rock can be observed simply with the aid of a hand lens. The structure of the minerals can be more easily distinguished with a microscope. For this, a section of rock is cut with a diamond-impregnated saw blade. Rock can be cut to a thin slice (typically 0.03 mm) to allow light to transmit though it. Polarized light is typically used. Two or three orthogonal sections may be required to reveal the complex three-dimensional structure of anisotropic rocks. More recent methods to observe the micro-structure of rock include: cathodoluminescence, laser-interference microscopy, SEM, TEM, X-ray tomography, computer-aided construction of three-dimensional images and X-ray compositional mapping [91].

## 2.12.  Outokumpu rock micro-structure

The mean modal and chemical compositions of the main minerals of the Outokumpu drill hole are listed by Västi [92]. A separate analysis for the lithology and chemical composition along the core samples from the Outokumpu drill hole along with the calculated modal compositions samples was reported by Kern [10].

The grain sizes for the Outokumpu core samples were reported by Västi: The mica schist grain size is typically less than 0.6 mm with the largest biotite flakes at 1.5 mm. In biotite gneiss, which typically shows veined structure, the length of biotite flakes is up to 4 mm, while plagioclase and quartz grains are less than 1.5 mm. In chlorite-sericite schist the grain size is typically less than 0.6 mm and it shows no evidence of relict primary structure. The maximum size of honblende grains is near 3 mm. The quartz grains are 0.1-5 mm in size and nematoblastic tremolite and diopside needles are typically shorter than 1 cm [92]. Additionally Hölttä and Karttunen report the grain sizes as a function of depth in [93].

A general extensive list of elastic properties of rock-forming minerals, including calculated properties of aggregates have been compiled by Simmons and Wang [94].

## 2.13.  Crystallization

Crystallization from solutions is a complex multistage process. The first stage requires supersaturation, a state of thermodynamic instability, defined as a difference between the actual concentration of the crystallizing solute and the saturation concentration. The supersaturation can be generated by various mechanisms, such as cooling, addition of anti-solvent, evaporation etc. The metastable zone width (MSZW) is the region between the solubility curve and the onset of nucleation (Figure 3). In other words, the difference between the saturation and spontaneous nucleation temperature. It defines the operating window during the crystallization process.

MSZW depends on several process dependent parameters such as cooling rate, solvent composition, stirring rate, crystallizer geometry etc. In the next stage the dissolved molecules begin to aggregate to relieve the supersaturation and move the system toward equilibrium. This leads to nucleation which means the formation of nuclei that act as centers of crystallization. The process is dynamic: new nuclei form and old dissolve. The induction time ($t_{ind}$) is the elapsed time between reaching supersaturation and the appearance of crystals. A nucleus is the minimum amount of new phase capable of independent existence. The nucleation leads to growth stage, which is governed by the diffusion of molecules to the surface of the existing nuclei and their embodiment into the crystal lattice. This continues until all excess solute is consumed. Crystal growth is a dynamic process where molecules also dissolve back into solution. The initial stages of crystallization between the supersaturation and formation of nuclei, determines largely the properties of the arising particles, such as purity, crystal structure and particles size [95]–[98].
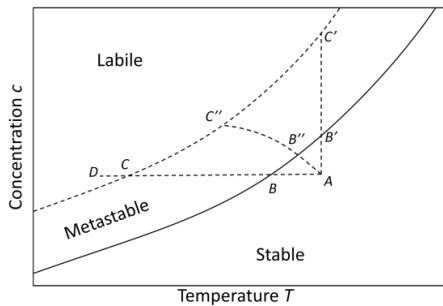


Figure 3. The solubility-supersolubility diagram is divided into three regions. (1) In the stable zone crystallization is impossible. (2) In the metastable zone crystal growth will continue but spontaneous crystallization is improbable. (3) In the labile supersaturated zone spontaneous crystallization is probable. Crystallization can occur via cooling (line *ABC,* sometimes requiring *D*), evaporation (*AB'C'*) or combination of them (*AB''C''*). Adapted from [98].

Classical nucleation theory (CNT) states that the kinetics of the nucleation are governed by changes in the Gibbs energy. Two opposing forces drive the nuclei towards growth or dissociation. These forces are size dependent. If the nucleus size is smaller than the critical size, it shrinks spontaneously. If it reaches a size that is larger than the critical size, it will grow. The requirement for the crystal growth is the gain in free energy $\Delta G$. Crystal formation takes place only if $\Delta G<0$ [99], [100].

For spherical nuclei of radius $r$, the $\Delta G(r)$ is

$$\Delta G(r) = \frac{4}{3}\pi r^3 \Delta g + 4\pi r^2 \gamma, \tag{59}$$

where the first term describes the volume contribution and $\Delta g$ is the driving force for precipitation per unit volume i.e. the free energy difference between nucleated and non-nucleated phases. The second term describes the interface between the nucleus and the surroundings and $\gamma$ is the surface tension. The first term is typically negative and second always positive. The interface term dominates at small $r$ and as it increases the volume term starts to dominate (Figure 4). The critical nucleus size occurs at d$G$/d$r$=0:

$$r^* = -\frac{2\gamma}{\Delta g}. \tag{60}$$

The minimum work $\Delta G^*$ required to form a stable nucleus of size $r^*$ is

$$\Delta G^* = \frac{16\pi\gamma^3}{3(\Delta g)^2}. \tag{61}$$

[101], [102].
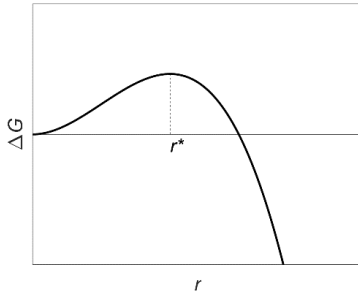


Figure 4. Gibbs energy changes according to the size of the forming nucleus. The critical radius for stable nucleus is $r^*$. Adapted from [99], [102].

The expression for nucleation rate $J$ is:

$$J \propto \exp\left(\frac{-\Delta G^*}{k_B T}\right), \tag{62}$$

where, $k_B T$ represents the Boltzmann constant with absolute temperature $T$ [103].

## 2.14.    Sonocrystallization

When the amplitude of acoustic wave propagating in liquid is increased sufficiently, the negative pressure exceeds the local tensile strength of the liquid. This leads to cavitation, where bubbles are formed. Because the bubbles cannot be sustained without absorption of energy, they collapse implosively after reaching the resonant size. This phenomenon is called acoustic cavitation.

The wavelength ($\lambda$) of ultrasound in liquid depends on the velocity ($v$) and frequency ($f$)

$$\lambda = \frac{v}{f}. \tag{63}$$

and is typically in mm- to cm-scale, much larger than the molecular size scale. Thus, ultrasound does not directly affect the molecules, but the interaction happens through the cavitation process. The implosion of the cavitation bubbles creates hot spots, which have intense local temperatures (~5000 K), pressures (~1000 bar) and a rapid heating and cooling rate ($>10^{10}$K s $^{-1}$). This also produces shockwaves (~4000 m/s), which can

directly interact with particles, causing breakage called sonofragmentation and high-velocity interparticle collisions.

The behavior of a bubble in liquid can be viewed as an oscillatory system. A spherical bubble can be described with its radius varying in time $R(t)$. The bubble radius at rest is $R_n$, external pressure in the liquid $p_e$, pressure inside the bubble $p_i$, polytropic exponent of the gas in the bubble $\kappa$ and $\rho$, $\mu$ and $\sigma$, the density, the dynamic viscosity and the surface tension of the liquid, respectively. The basic model is the Rayleigh model

$$\rho R\ddot{R} + \frac{3}{2}\rho\dot{R}^2 = p_i - p_e, \tag{64}$$

where an overdot represents differentiation with respect to time. The difference between the internal and external pressure $p_i$-$p_e$ drives the bubble motion. Both, $p_i$ and $p_e$, become functions of radius $R$ and time $t$, when the bubble becomes filled with gas and vapor, and when surface tension $\sigma$, liquid viscosity $\mu$ and sound field, $p(t)$, are taken into account. When these are considered, the Rayleigh model becomes:

$$\rho R\ddot{R} + \frac{3}{2}\rho\dot{R}^2 = p_{gn}\left(\frac{R_n}{R}\right)^{3\kappa} + p_v - p_{stat} - \frac{2\sigma}{R} - \frac{4\mu}{R}\dot{R} - p(t), \tag{65}$$

with

$$p_{gn} = \frac{2\sigma}{R_n} + p_{stat} - p_v, \tag{66}$$

where $p_{gn}$ is the gas pressure inside the bubble at rest, $p_{stat}$ the static pressure and $p_v$ the now constant vapor pressure. The pressure $p(t)$ is an external force exerted on the bubble wall, which in the case of ultrasonic excitation at a single frequency of $v_a$ and pressure $p_a$, can be written in the form

$$p(t) = -p_a \sin(2\pi v_a t). \tag{67}$$

The application of ultrasound can reduce the induction time, supersaturation and MSZW and can thus be used to control nucleation [18], [104]–[106]. Possible mechanisms for these have been presented in the literature such as the direct effect of high pressure arising around cavitation bubbles, or the effect of rapid local cooling rates. Alternative hypothesis is based on the molecular segregation of a liquid mixture by the cavitation bubbles. When a mixture of two species is submitted to a pressure gradient, the lighter substance is pushed toward the low-pressure regions. As the outward acceleration of the collapsing bubble is about twelve orders of magnitude higher than gravity, it is conceivable that the corresponding pressure gradient can segregate the species present in the liquid [107].

# 3. METHODS

## 3.1. Uniaxial apparatus

Custom ultrasonic transducers were built to transmit stress and ultrasonic signals in a through-transmission configuration to cylindrical rock samples of two different sizes (25 mm diameter, 20-25 mm height and 40 mm diameter, 30-70 mm height). The transducer housing was machined of stainless steel. To incorporate a void for piezoceramics and water channels for optional cooling, the transducer housing was machined from two pieces and bolted together. O-rings were used in sealing the water channel. A longitudinally polarized disc (1.0 MHz nominal frequency, D = 5 mm, h = 2 mm) and a shear plate (1.1 MHz nominal frequency, L = 5 mm, W = 4 mm, h = 0.8 mm) of Pz27 piezoceramic (Ferroperm) were fixed inside the transducer with silver epoxy (CW 2004, Circuit Works). The signal wires were soldered to the electrode surfaces and to BNC-connectors attached to the transducer housing (Figure 5).
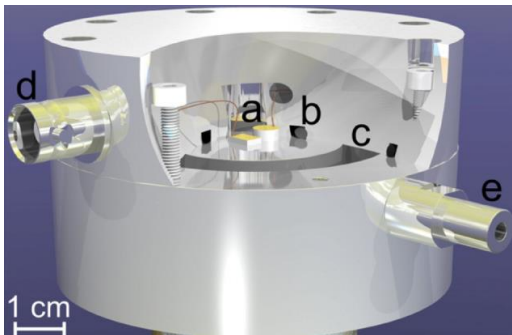


Figure 5. Illustration of the ultrasonic transducer, with a partly cut-out view of the upper part, shows the interior of the transducer with piezo elements (a), O-ring seals (b) and a water-cooling channel (c). On the left-hand side of the transducer is a BNC-connector (d) for the shear wave piezo and on the right-hand side is a water inlet (e) for optional cooling. On the opposite sides (not visible in the picture) are the BNC-connector for the longitudinal mode piezo and the water outlet.

The Pz27 piezoceramic material (Navy II) is a general purpose material for NDT applications with low mechanical Q-factor [108]. To increase the bandwidth and reduce the ringing, the ceramics were backed with a mixture of tungsten powder and epoxy. This mechanical damping shortens the impulse response of the transducers. The disadvantage of the backing is that it absorbs energy which would otherwise be transmitted to the sample [109].

In order to apply uniaxial stress onto rock samples a single acting hydraulic cylinder (HSS 254, Hi-Force) with 25-ton (245 kN) capacity, 102 mm stroke and spring assisted return was installed inside a steel frame capable of carrying 40-ton load. A hydraulic 3-way, load holding pump (HEP 2142S3, Hi-Force) was used to drive the cylinder. The

pump was controlled by a PC through DAQ-card (PCI-6024E, National Instruments) and a relay circuit (Figure 6).

To prevent the samples from breaking under compression, they were measured while enclosed inside a two-piece brass ring sample holder, that was a slightly shorter than the sample (Figure 7). All measurements were performed using the sample holder. The applied force was monitored with a load cell (Model 53, Honeywell) that converted the compressional force to an electrical output that was amplified with a load cell amplifier (7528, Lebow) and recorded with the DAQ-card. The maximum nonlinearity of the load cell was 60 kg. The load cell can monitor force up to 23 ton (222 kN). The deformation of sample during compression was measured with a linear gage (543-250B, Mitutoyo) (1 μm resolution, 3 μm accuracy) attached to the side of the transducer. The reading was recorded with the DAQ-card. Sample temperature was measured with a thermocouple through a hole in the sample holder.

A high voltage pulser-receiver (5058PR, Panametrics) was used to excite ultrasonic transducer (max 900 V voltage) and amplify the received signals with up to 60 dB gain with additional 30 dB internal auxiliary preamplifier. The signals were then sampled at 50 MS/s, averaged (300 times, summed average) and recorded with an oscilloscope (9410, LeCroy, 150 MHz bandwidth, 8 bit resolution). The duration of the captured waveforms was 50 μs that resulted in 2500 data points per channel. The compressional load was constant (±100 N) during the signal acquisition.

The received ultrasonic signals, measured load, sample deformation and sample temperature were recorded with a PC running LabVIEW that also controlled the hydraulic pump. The data was then analyzed with Matlab. The time of flight (*ToF*) for *P*- and *S*-waves was determined from the first peak of the interpolated signal. Reference values for *ToF*s without a sample were recorded before the actual measurements. The *Vp* and *Vs* were obtained by dividing the sample length including the deformation with the *ToF* through the sample.



Figure 6. The ultrasonic uniaxial rock measurement setup. A hydraulic cylinder is fixed to the top of the steel frame inside which the transducer-sample assembly resides. A load cell- and thermocouple-amplifiers are placed on the right side of the frame. The hydraulic motor and relay control unit are behind the oscilloscope and pulser/receiver. The PC and the optional cooler and oven are outside the picture.
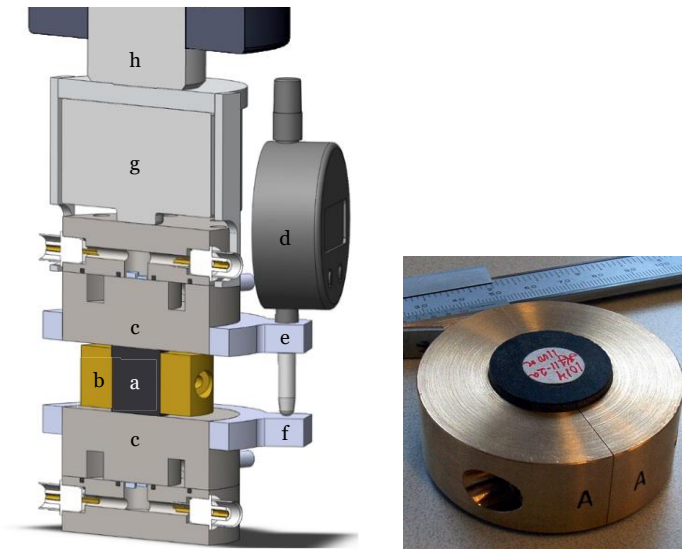
Figure 7. Left: The 25 mm diameter sample (a) resides inside the brass sample holder (b) between the transducers (c). The linear gage (d) is attached to the holder (e) and sensing element is touching the counterpart (f). The load cell (g) is attached to the piston (h). Right: A cylindrical 25 mm diameter rock sample mounted inside a two-piece brass sample holder held together with M6 bolts.

## 3.2. Stress field in rock

To estimate the stress state of a rock sample inside a sample holder under uniaxial compression, finite element method (FEM) simulations were performed using static analysis in SolidWorks software. The simulated rock sample had 25 mm diameter and 22 mm height. The generalized material properties for rock used in the calculations were $E$ = 65 GPa, $v$ = 0.25, $\rho$ = 2800 kg/m³ and yield strength = 20 MPa, based on average mechanical properties of measured rocks [110]. The brass sample holder had 25 mm inner diameter, 35 mm outer diameter and 20 mm height with material properties $E$ = 100 GPa, $v$ = 0.33, $\rho$ = 8500 kg/m³ and yield strength = 240 MPa. The stainless-steel transducer had 60 mm diameter and 50mm height. The material properties were $E$ = 193 GPa, $v$ = 0.3, $\rho$ = 8000 kg/m³ and yield strength = 138 MPa. The simple model assumed linear, elastic, and isotropic material. The simulations were performed using symmetry boundary conditions by splitting the model in four with orthogonal vertical planes and in half with horizontal plane (Figure 8). This reduced the required calculations and bounded the geometry in place. The geometry was discretized using solid mesh with 0.8 mm element size. A 15 kN force was applied on the upper transducer top surface.
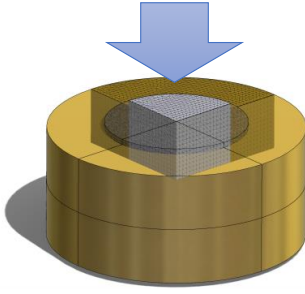
Figure 8. The stress state inside a rock sample was estimated using FEM simulations. One eight of the rock and sample holder geometry were meshed with 0.8 mm solid elements and symmetry conditions applied.

## 3.3. Multi-anvil apparatus

An apparatus was built to measure $V_p$ and $V_s$ (horizontal and vertical polarization with respect to propagation direction) simultaneously along three orthogonal directions in cubical (25 mm side) rock samples under compression. The configuration enabled to determine velocity anisotropy with a single measurement set without having to remove and realign the sample.

The transducers were machined of martensitic precipitation hardened stainless steel. The truncated pyramid shape consisted of two parts with spherical intersection. This allowed for slight shape deviations with the cube shaped samples (25 mm side). The contacting surface was smaller (24 mm side) than the sample to allow sample size variation and compression. Three Pz27 piezo ceramics (Ferroperm) were attached to a plane on the otherwise spherical surface with silver epoxy (CW 2004, Circuit Works): one longitudinally polarized disc (1.0 MHz nominal frequency, D = 5 mm, h = 2 mm) and two perpendicularly oriented shear plates (1.1 MHz nominal frequency, L = 5 mm, W = 4 mm, h = 0.8 mm). The signal wires were soldered to the electrode surfaces and the coaxial cables run in channels on the backside of the transducer to BNC-connectors, one for each piezo. The mixture of tungsten and epoxy backing material also incorporated a spring through which steel wires were inserted to hold the two pieces together.

Three low profile hydraulic cylinders (HVL20, Hi-Force, 180 kN, 6 mm stroke length) were used for loading the sample in three directions. The cylinders were operated by an electric driven hydraulic pump (HEP2132S-3, Hi-Force). As same pressure was applied in all directions, the load was monitored with a single load cell (Model 53, Honeywell/Sensotec) connected to a load cell amplifier (7528, Lebow). The compression of the sample was monitored with three linear variable differential transformers (LVDT) (ORBIT 3 DP/10/S, Solartron) (0.15 µm repeatability, <0,1 µm resolution). DAQ-card (USB 6008, National Instruments) connected to a PC was used for reading the load cell amplifier and controlling the pump.

A multiplexer circuit was built to control the timing for the pulses by triggering the pulser receiver and switching the active piezoceramics. The transmitted signals were switched with electromechanical relays (MI-SH-212L, Goodsky) while solid-state CMOS analog switches (DG 417 and DG 419, Vishay) were used for the received signals. With the multiplexer circuit, a single pulser receiver (5085PR, Olympus

Panametrics) could be used in exciting the transducers and amplify the received signals that were then acquired with oscilloscope (9410, LeCroy) and stored with PC using LabVIEW (National Instruments) (Figure 10). The data was then analyzed with Matlab.

The transducers and hydraulic cylinders were attached in a steel frame where the top part was hinged so that the sample could be inserted between the transducers.
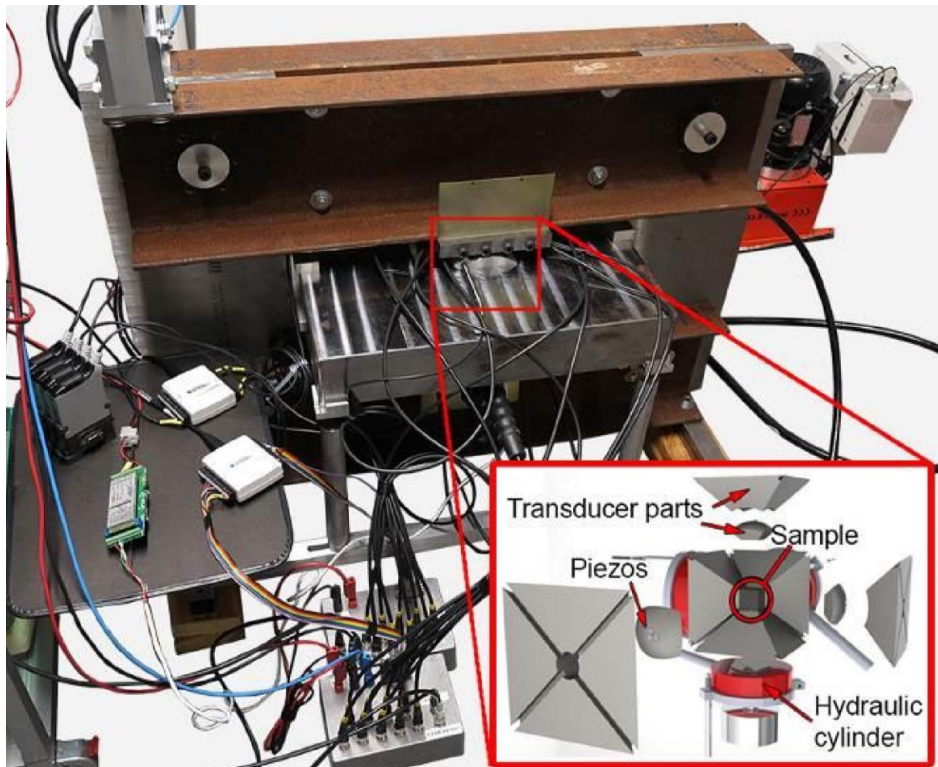


Figure 9. Exploded view of the transducer assembly (inset) and the steel frame that supports the transducers. The electronics consist of LVDT modules, DAQ-cards, load-cell amplifier and multiplexer circuits.
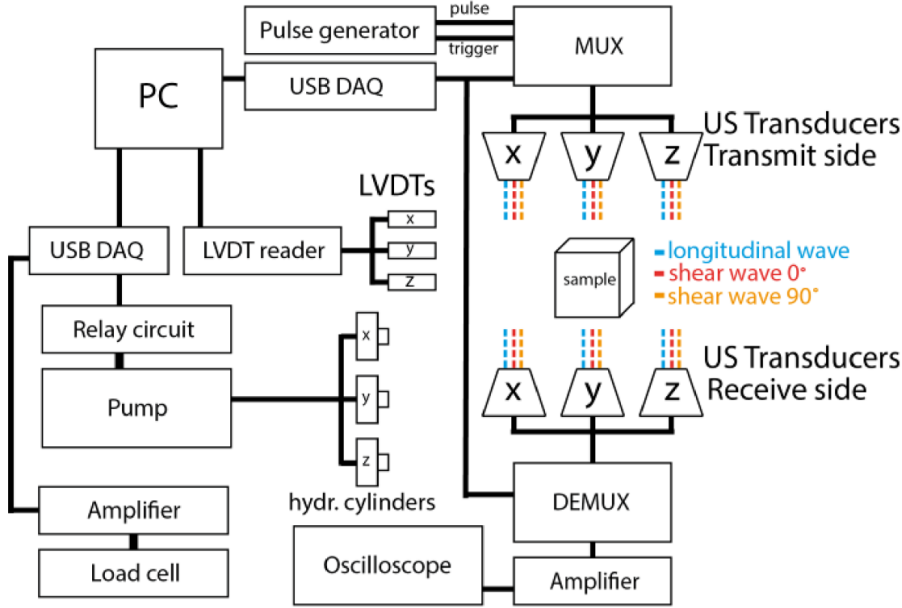
Figure 10. The multi-anvil measurement configuration showing the devices and connections.

## 3.4. Preparation

The measured cylindrical core samples had parallel ends that were sanded smooth to ensure good contact to transducers. The sample height $h$ was measured with a Vernier caliper five times and the average and standard deviation values were recorded.

The internal delays of the system $ToF_{reference}$ that are caused by the transmitting and receiving electronics and the propagation times through the transducer internal structures were measured before the sample measurements. The $ToF_{reference}$ was determined from the first peak of the received signal. Similarly, the $ToF_{total}$ was later determined including the sample from the corresponding peak albeit delayed and with lower signal to noise ratio.

To include the transducer compression under pressure, reference steel samples of same width as the rock samples and different lengths were measured. The $ToF_{reference}$ was also verified with a pulse echo measurement from the transducer front face reflection under similar load cycle that was used with samples. After the measurement the $ToF$ through the sample could be obtained by subtracting the $ToF_{reference}$ from the $ToF_{total}$.

Velocities $V_p$ and $V_s$ were calculated from measured $ToF$ and sample height $h$ taking into account the sample compression $\Delta h$

$$V = \frac{h - \Delta h}{ToF_{total} - ToF_{reference}}. \tag{68}$$

34

Identifying the *S*-wave can pose a challenge, as mode conversion can occur when a wave encounters interface. Also, the coupling of the shear wave requires sufficient contact force. In some cases, the *S*-wave was not clearly recognizable from *P*-wave at low pressure. At higher pressure the *S*-wave became more dominant and the corresponding peak could be followed to lower pressures. One way of identifying the *S*-wave was to rotate the transducers. When the transducers were aligned at 90° the S-wave should not be present and at 180° it should be at opposite phase.

## 3.5. Ultrasonic measurements in Paper I

The upper schist series (also referred to as the upper gneiss series) (33-1314 m) in the Outokumpu deep drill core consists mostly of strongly foliated fine-grained biotite gneisses and mica schists with chlorite-sericite and black schist interlayers. There is generally gradual transition between these. [10], [92]. This is mineralogically uniform area and features uniform elastic wave velocity distribution. Consequently, this section offered relevant samples to compare the uniaxial apparatus to a multi-anvil apparatus described in literature [10]. The samples were measured under 0-300 MPa stress, dry, at room temperature (22°C). The moisture content (<0.03%) was determined from the sample weight change and the dry weight was measured after drying at 80°C for five days. Additionally, 105 water saturated (immersed in tap water for 3 days) samples originating from 125-1705 m depth and measured under 30 MPa stress were compared to z-direction (along the core) velocities in dry samples from the same bore hole from 578-1845 m under triaxial pressure in a multi-anvil apparatus under 25-35 MPa to examine the effect of water saturation.

## 3.6. Ultrasonic measurements in Paper II

Over 100 samples were water-saturated to simulate the conditions in the upper crust. The applied stress was chosen according to the sample depth (125-1500 m). Because of the subsurface temperature (increasing only up to 40°C at the final 2.5 km depth) and mainly insignificant temperature dependence observed in tests, the velocity measurements were conducted at room temperature (20°C) altering only the stress.

## 3.7. Ultrasonic measurements in Paper III

Water saturated and dry samples were measured in ambient laboratory conditions and under both increased temperature (up to 300°C) and pressure conditions (up to 120 MPa, corresponding to a depth of 4.5 km), where the temperature and stress were varied simultaneously. Two sample sizes were measured: 25 mm diameter cylinders with ~25 mm height and 40 mm diameter cylinders with 30-70 mm height.

## 3.8. Ultrasonic measurements with multi-anvil setup

Eleven rock samples from FIRE reflection line were prepared to cube shape (~25 mm side) and polished (Ylämaan korukivi Ky) (Figure 11). The reference *ToF* values for each of the three transducer pairs of the multi-anvil apparatus was measured face-to-face without external delay line. Ultrasonic *ToF* was then measured for the rock samples. The measurements were done along three perpendicular (X, Y and Z) directions. The stress was increased up to 102 MPa (corresponding to ~3 km depth).



Figure 11. Precambrian rock samples from FIRE-seismic line. The four samples on the bottom (#107, #111, #135 and #138) were selected for detailed study.

## 3.9. Porosity measurements

The ceramic samples were manufactured at the University of Art and Design Helsinki. A clay mixture was prepared from 40% feldspar (FFF K7), 30% kaolin (Grolleg ECC), 20% ball clay (Hyplas 64) and 10% quartz (FFQ). The mixture was prepared to cylinders of ~10 cm height and diameter and fired in a kiln at 1000-1200°C for 6-8 hours. Increased firing temperature reduced the porosity of the ceramic samples (Table 6). Cylindrical core samples (25 mm height and diameter) were cut from fired ceramics and the parallel faces were polished.

The *ToF* of ceramic cylinder samples was determined using ultrasonic through transmission technique. The samples were placed between two horizontally mounted transducers: longitudinal (S 24 HB 0.3-1.3MHz, Karl Deutch) for determining $V_p$ and shear (3.2-4.2 MHz -6 dB bandwidth, custom) for $V_s$. The transducer sample assembly was loaded from the top with a 9.81 N force using 1 kg lead block to ensure the contact between the sample and transducers. Reference *ToF* for longitudinal signals was determined using 20 mm long fused quartz cylinder between the transducers. The shear wave transducers featured internal delay lines, so reference *ToF* could be obtained without separate delay line.

## 3.10. Sonocrystallization experiment

The aim was to control polymorph formation in semi-batch crystallization of $L$-glutamic acid from a monosodium glutamate solution with sulfuric acid ($H_2SO_4$). $L$-glutamic acid exhibits two polymorphs: metastable α-polymorph, which forms prismatic or granular crystals and stable β-polymorph, which forms needle or flake shaped crystals.

The experimental setup consisted of a cylindrical 50 l jacketed glass crystallizer of 300 mm diameter with semispherical bottom, four 30 mm baffles, and an up-flow 6 blade turbine (150 mm diameter) (Figure 12).

The crystallizer temperature was kept at 25°C with a thermostat (Integral T4600, Lauda). A 13.05 dm³ initial batch of 1.5 M monosodium glutamate (99%, Sinochem Ningbo Ltd.) was employed. Next 7 dm³ of 1.5 M sulfuric acid (95-97% pro analysis, Merck) was pre-cooled to 10°C. The acid was then fed with peristatic pump (5 g/s) through a 2 mm nozzle into the crystallizer until the preset supersaturation level was reached. The feed rate was feedback controlled from the concentrations of glutamic acid and glutamate, determined from ATR-FTIR spectrum [111].

The controlled pre-nucleation supersaturation set values were 0.7 M and 1 M. With spontaneous nucleation, the addition commenced when the increase in pH was detected, whereas with seeding, nucleation was initiated by addition of seed crystals. Power ultrasonic nucleation was initiated with 20 min (0.7 M set value), 11 min and 1 min (1 M set value) sonication times (30% of 600 W electric power) using 20 kHz ultrasonic processor (VCX 600, Sonics and Materials). The ultrasonic radiation was directed in the feed nozzle area by means of a tapered microtip (3 mm diameter, titanium alloy). Following the start of nucleation, the supersaturation set value decreased linearly as a function of added sulfuric acid.

Suspension samples were taken from the batch when the nucleation was observed, 10 min after nucleation, at the end of the batch experiment and 30 min after the end during continued mixing. The suspensions were filtered and washed with ethanol (Etax Aa, 99.5 wt%, Altia) to retrieve the crystals. The particle size distribution (PSD) and polymorph content were determined by laser diffraction sizing analyzer (LS13320, with Tornado dry powder system, Beckman Coulter) and by Raman spectroscopic microscope (LabRam 300, Horiba Jobin Yvon), respectively. Scanning electron microscope (SEM) (JSM-5800, JEOL, 20 kV acceleration voltage, gold coated sample) was used to determine the crystal shapes.
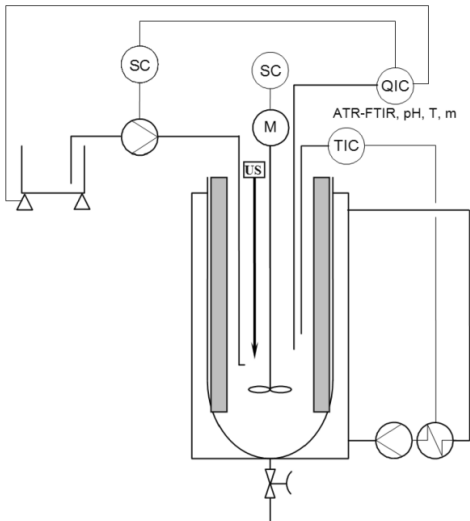
Figure 12. The experimental setup for supersaturation controlled semi-batch crystallization of *L*-glutamic acid consists of a crystallizer, thermostat circuit, ultrasonic liquid processor and feed pump. The feed flow of sulfuric acid (from the left) was controlled by closed control loop monitoring the ATR-FTIR spectra, pH and mass of sulfuric acid to be fed.

# 4. RESULTS

## 4.1. Stress field in rock

Without the sample holder the FEM simulation predicted 300 MPa axial stress and virtually no radial and tangential stresses when the rock was loaded with 15 kN force. The addition of the sample holder complicated the stress field. Contact type between the rock, transducer and sample holder affected significantly the resulting stress field. Because it is difficult to estimate the friction between the parts under load, three contact set cases were studied: sliding, 0.5 friction coefficient, and bonded. The stress fields were plotted in cylindrical coordinates using section plots for the chosen contact types in Figure 13.

The effect of the sample holder was observed on the rock surface and inside it. The sample holder reduced the axial stress while increasing radial and tangential stress components. Large stress values were present at the surfaces of the rock, either at the edge or at the side next to the sample holder edge, especially with bonded contacts. In case of 0.5 friction coefficient, fluctuations of stress components were observed at the surface in contact with the transducer.
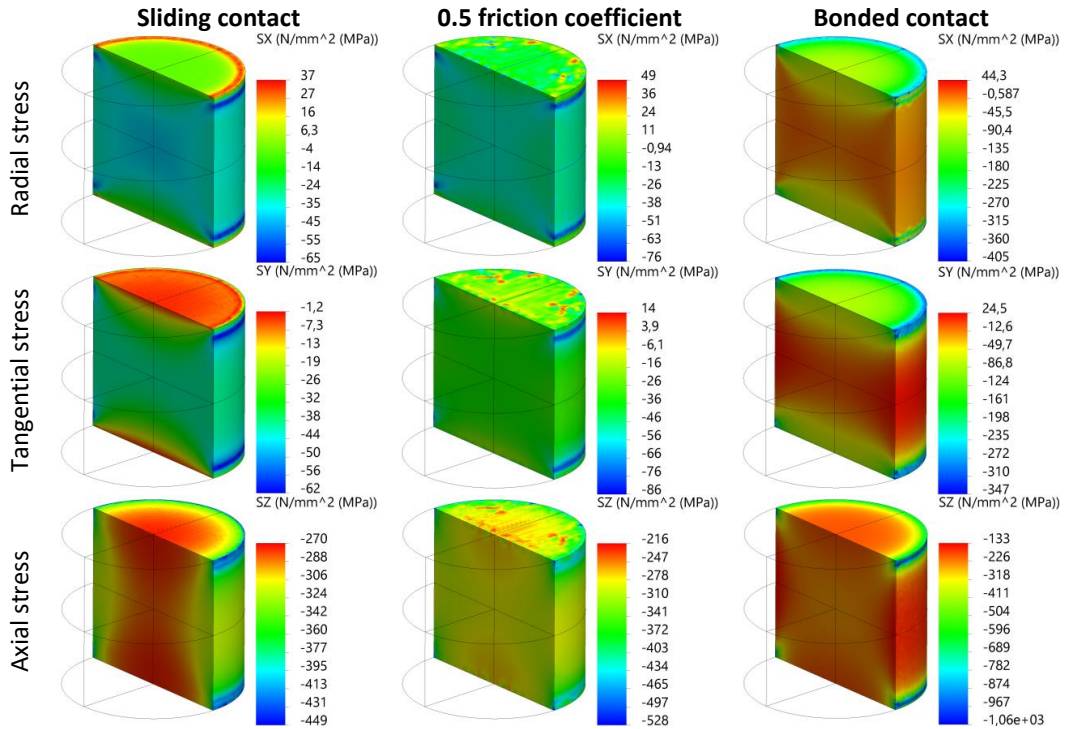
Figure 13. The stress distribution in radial, tangential, and axial direction for simulated rock inside a sample holder with different contacts (no friction, 0.5 friction coefficient and bonded) between the rock, sample holder and the transducers, when the rock is loaded with 15 kN axial force.

The radial, tangential and axial stresses along the center axis from the rock top surface to its center are presented for different contact types in Figure 14. The radial stress increases from near zero, in case of sliding contact, or from around -20 MPa, with 0.5 friction coefficient case, to around -40 MPa at the center of the rock. In case of bonded contact, the radial stress reduces from -85 MPa to zero. With tangential stress, the trends are similar. With sliding contact and 0.5 friction coefficient the stress increases to close to -40 MPa at the center of the rock. Sliding contact case yielded the smallest radial and tangential stress components and subsequently largest axial stress. The axial stress starts from around -270 MPa in sliding and 0.5 friction coefficient case and -190 MPa in bonded case and increases towards the center of the rock reaching around -280 MPa and -250 MPa respectively.
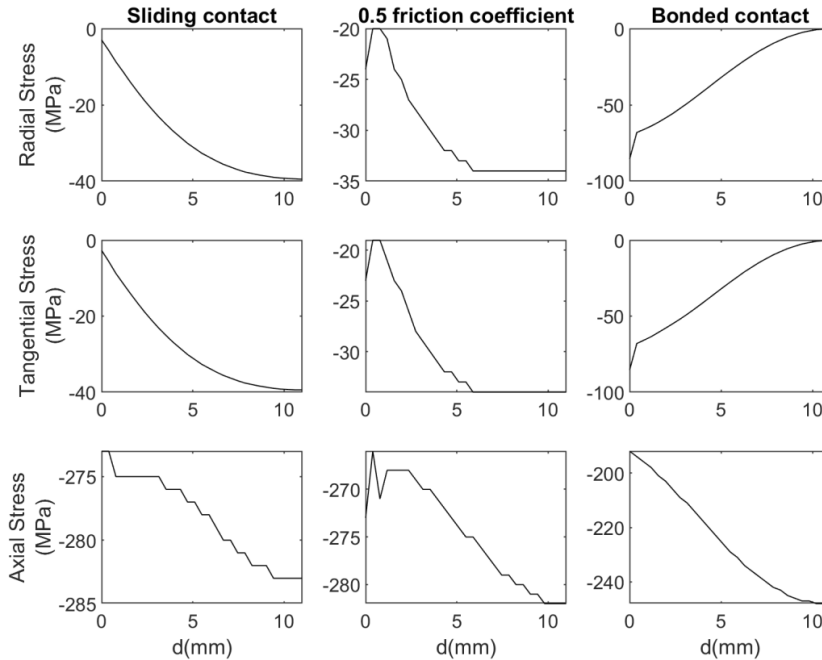
Figure 14. Radial, tangential and axial stresses from the top of the rock (d=0 mm) to its center (d=11 mm) along the axis calculated with different contact types (no friction, 0.5 friction coefficient and bonded) between the rock, sample holder and the transducers, when the rock is loaded with 15 kN axial force. The 0.5 friction coefficient was estimated to be more realistic than the other contact types.

The reported pressure values in the following sections neglect the sample holder effect, because the sample holder effect was studied later. The stress state inside the rock under compression is not uniaxial. Radial and tangential stress components rise because the sample holder supports the expanding rock. The FEM simulation results can help to estimate the actual stress field of the setup.

## 4.2. Dry samples

The mean values and standard deviations of the $Vp$ and $Vs$ start from 4100±500 m/s and 2600±200 m/s at 5 MPa uniaxial loading (equivalent to pressure at 170 m depth), increase to 5020±300 m/s and 2890±100 m/s at at 25 MPa (~880 m depth) after which the velocity increase slows down to 5520±130 m/s and 3270±60 m/s at 300 MPa (~10 km) (Table 1). The coefficient of variation (CV), which is the ratio of standard deviation ($\sigma$) to the mean ($\mu$), decreases with increasing pressure from 11% and 7% down to 2% for $Vp$ and $Vs$ respectively.

Table 1. *P*- and *S*-wave velocities of dry mica schist samples from Outokumpu core section (774 m – 920 m depth) under 5-300 MPa stress measured using uniaxial apparatus.

| | Depth (m) | 5 MPa | 25 MPa | 35 MPa | 50 MPa | 100 MPa | 200 MPa | 300 MPa | $\rho$ (kg m$^{-3}$) |
|---|---|---|---|---|---|---|---|---|---|
| $Vp$ (m/s) | 774 | 4760 | 5390 | 5490 | 5570 | 5660 | 5690 | 5700 | 2744 |
| | 784 | 3800 | 4950 | 5080 | 5180 | 5330 | 5420 | 5470 | 2739 |
| | 867 | 4530 | 5250 | 5340 | 5430 | 5510 | 5560 | 5610 | 2738 |
| | 876 | 4140 | 5030 | 5160 | 5270 | 5400 | 5500 | 5560 | 2722 |
| | 912 | 3870 | 4890 | 5040 | 5170 | 5330 | 5430 | 5480 | 2719 |
| | 920 | 3490 | 4630 | 4800 | 4940 | 5090 | 5230 | 5310 | 2755 |
| $Vs$ (m/s) | 774 | 2710 | 2960 | 3010 | 3070 | 3150 | 3210 | 3230 | 2744 |
| | 784 | 2420 | 2850 | 2890 | 2930 | 3100 | 3250 | 3290 | 2739 |
| | 867 | 2820 | 3020 | 3080 | 3150 | 3210 | 3290 | 3340 | 2738 |
| | 876 | 2610 | 2940 | 3000 | 3070 | 3170 | 3270 | 3330 | 2722 |
| | 912 | 2330 | 2750 | 2820 | 2900 | 3050 | 3140 | 3170 | 2719 |
| | 920 | 2490 | 2810 | 2890 | 2980 | 3130 | 3240 | 3270 | 2755 |

Results are compared with velocities obtained with multi-anvil in z-direction for samples from the same Outokumpu core section [10]. At 25 MPa the uniaxial measurements 5020±300 m/s exceed multi-anvil results 4720±300 m/s by 300 m/s. With increasing pressure, the uniaxial $Vp$ values approach the multi-anvil results and at 300 MPa they differ by 10 m/s.

At 25 MPa stress the uniaxial $Vs$ values are 2890±100 m/s compared to multi-anvil values of 2990±110 m/s. The difference is largest at 35 MPa where the uniaxial $Vs$ values are 2950±100 m/s compared to multi-anvil values of 3090±110 m/s. With increasing pressure, the difference decreases and at 300 MPa the uniaxial $Vs$ is 3270±60 m/s whereas the multi-anvil $Vs$ is 3310±90 m/s. The CV decreases with increasing pressure in both cases (Figure 15).
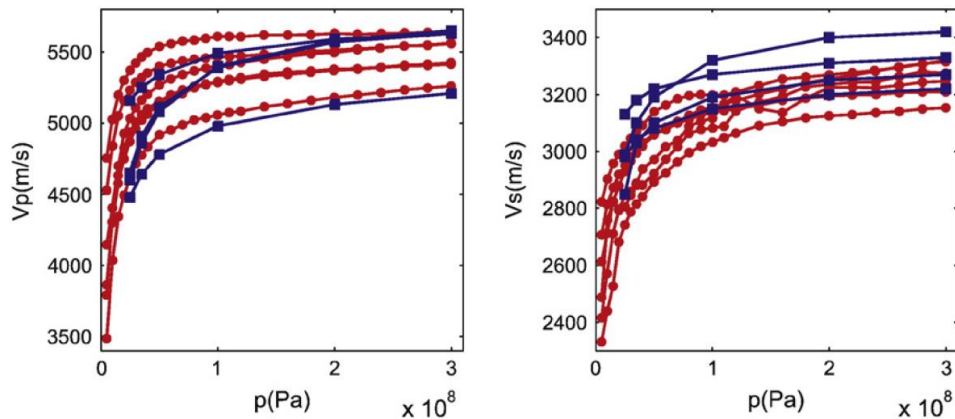


Figure 15. *Vp* and *Vs* values of dry mica schists (depths: 774 m, 784 m, 867 m, 876 m, 912 m, 920 m; red dots) measured with uniaxial apparatus (this study) and with multi-anvil (depths: 578 m, 676 m, 818 m, 1093 m; blue squares) [10] as a function of applied stress. Both velocities increase with increasing pressure. The measured *Vs* values in this study were 40 m/s slower (at 300 MPa). Velocity values are connected with lines for clarity. Closing of the microcracks occurs at the nonlinear part of the velocity graph below 100 MPa pressure.

## 4.3. Water saturated and dry samples at 30 MPa

To examine the effect of water saturation, velocities of 105 water saturated samples measured with uniaxial configuration were compared with velocities of 13 dry samples, representing major lithologies, measured in z-direction with multi-anvil (Figure 16). The *Vp* for water saturated samples was 5500±240 m/s and *Vs* 3100±240 m/s obtained uniaxial setup, whereas dry values with multi-anvil where *Vp* 5100±800 m/s and *Vs* 3100±500 m/s. Limiting the comparison to the relatively uniform upper gneiss (33-1314 m depth) series as with dry samples the mean velocities and standard deviations were 5500±200 m/s and 3200±200 m/s for uniaxial *Vp* and *Vs* respectively, whereas reported *Vp* and *Vs* values with multi-anvil configuration were 5100±800 m/s and 3100±500 m/s.
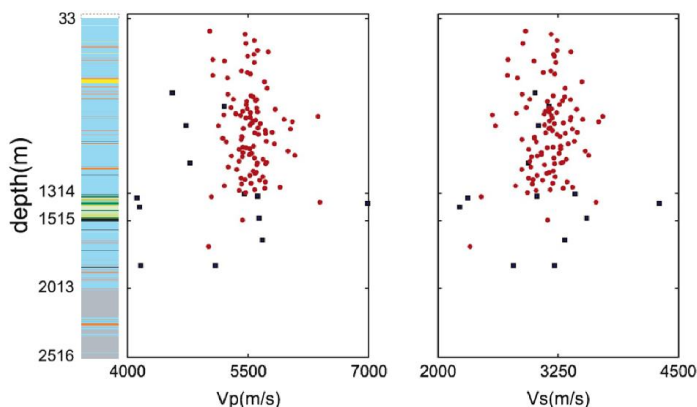


Figure 16. *Vp* and *Vs* values of saturated samples measured with uniaxial apparatus (red dots, this study) and dry samples measured multi-anvil (blue squares, [10]). Water saturation affects the *Vp* values, whereas *Vs* is insensitive to it. The colorbar on the left marks the sample lithology as in Figure 1.

## 4.4. Seismic velocities at *in situ*-like pressure conditions

The *Vp* and *Vs* values obtained under *in situ* conditions varied considerably (Figure 17). The average *Vp* and *Vs* for the upper schist series were 5509 m/s and 3132 m/s, respectively. The variation in the *Vp/Vs* ratio, ranged from 1.63 to 2.05, with more variation in the *Vs* than *Vp*. The average *Vp/Vs* ratio for this series was 1.76. There was no depth dependence observed in *Vs*, but *Vp* increased slightly with depth. The Poisson's ratio ($v$) of these samples was 0.2-0.34 (0.26 on average). The seismic impedance ($Z_p$), calculated from the measured density and velocity data was on average 15.1 ×10$^6$ kg m$^{-2}$ s$^{-1}$ for the upper schist series and the corresponding Young's modulus ($E$) was 67.9 GPa. For the samples from ophiolitic complex (1314−1515 m) the average *Vp* was 5622 m/s, *Vs* 3076 m/s, *Vp/Vs* 1.85, $v$ 0.29, $Z_p$ 1.55 ×10$^6$ kg m$^{-2}$ s$^{-1}$ and *E* 67.1 GPa.

For mica schists the average values for *Vp* was 5501 m/s and for *Vs* 3124 m/s, *Vp/Vs* 1.77, $v$ 0.26, $Z_p$ 1.51 ×10$^6$ kg m$^{-2}$ s$^{-1}$ and *E* 67.5 GPa. For chlorite-sericite schist the *Vp* and *Vs* along with $Z_p$ and *E* were higher than for mica schists. *Vp/Vs* was 1.63 and $v$

0.20 for chlorite-sericite schist, whereas the biotite gneiss exhibited lower $Vp$ and $Vs$ ($Vp/Vs$ 1.83 and $v$ 0.29). The serpentinites differed the most from the other samples. They featured the highest $Vp/Vs$ of 2.06 and Poisson's ratio 0.35 together with the lowest impedance of 1.38 ×$10^6$ kg m$^{-2}$ s$^{-1}$ (Table 2).
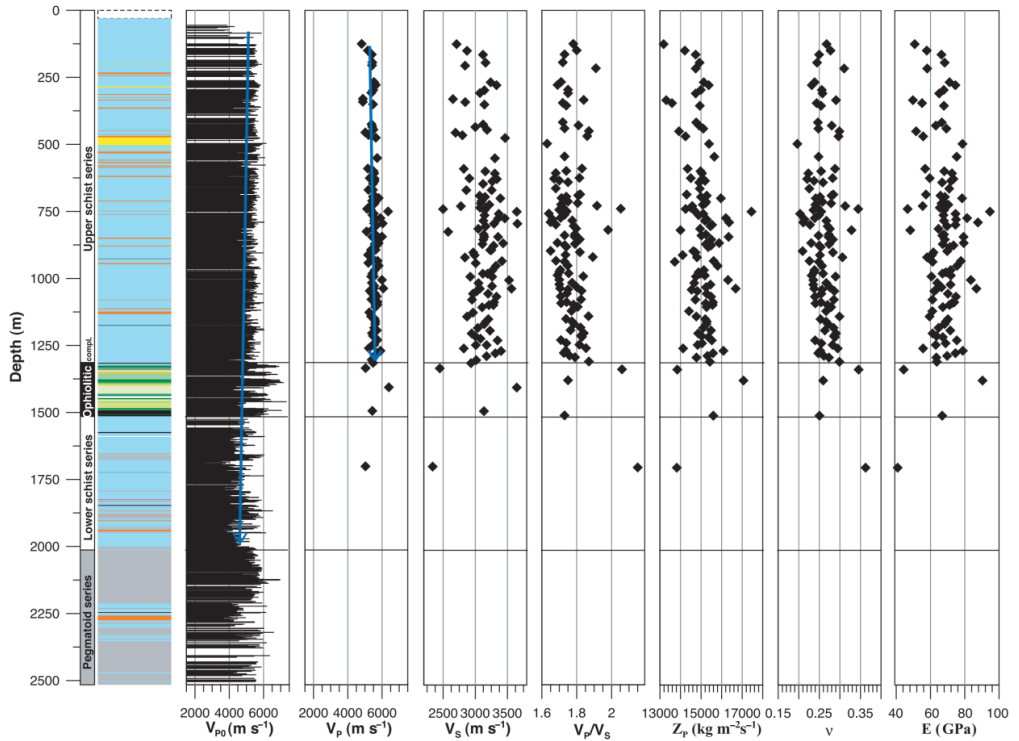


Figure 17. Seismic velocities *Vp* and *Vs*, their ratio *Vp/Vs*, acoustic impedance *Zp*, Poisson's ratio *v* and Young's modulus *E* of the upper schist series and ophiolite complex under *in situ* corresponding pressures. *Vp₀* values (bar chart) are measured in laboratory pressure conditions. Blue arrows indicate the increase of *Vp* and decrease of *Vp₀* with depth. The colorbar on the left marks the sample lithology as in Figure 1.

Table 2. Elastic properties of the lithologies in Outokumpu drill core. Values are average values of each lithology. Number of samples *n* (in brackets the number of samples used in *Vp₀*), *P*-wave velocity in ambient pressure measured in GTK *Vp₀*, *P*-wave velocity in *in-situ* conditions *Vp*, *S*-wave velocity in *in-situ* conditions *Vs*, *Vp/Vs* ratio, Poisson's ratio *v*, seismic impedance *Zp* and Young's modulus *E*. The highest velocities were observed with diopside-tremolite skarn and lowest with serpentinite. Serpentinite also features the highest *Vp/Vs* and Poisson's ratio and lowest acoustic impedance and Young's modulus.

| Lithology | $n$ | $V_{P0}$ (m s$^{-1}$) | $V_P$ (m s$^{-1}$) | $V_S$ (m s$^{-1}$) | $V_P/V_S$ | $v$ | $Z_P$ E$^6$kg m$^{-2}$s | $E$ GPa |
|---|---|---|---|---|---|---|---|---|
| Mica schist | 98 (1218) | 4919 | 5501 | 3124 | 1.77 | 0.26 | 1.51 | 67.5 |
| Biotite gneiss | 4 (107) | 4577 | 5367 | 2947 | 1.83 | 0.29 | 1.47 | 62.9 |
| Chlorite-sericite schist | 1 (18) | 5763 | 5636 | 3464 | 1.63 | 0.20 | 1.54 | 78.7 |
| Black schist | 1 (36) | 5577 | 5431 | 3134 | 1.73 | 0.25 | 1.56 | 66.8 |
| Diopside-tremolite skarn | 1 (35) | 6267 | 6395 | 3645 | 1.75 | 0.26 | 1.71 | 90.4 |
| Serpentinite | 1 (86) | 5054 | 5039 | 2448 | 2.06 | 0.35 | 1.38 | 44.3 |
| Serpentinite-tremolite-(olivine) rock | (15) | 6266 | - | - | - | - | - | - |
| Quartz | (5) | 5830 | - | - | - | - | - | - |
| Pegmatite granite | (256) | 5396 | - | - | - | - | - | - |

Reflection coefficients were calculated using velocities measured under crustal conditions (Table 3). Contacts between the diopside-tremolite skarns and mica schists

($R_c$ = 0.126; 1325.4 m), diopside-tremolite skarns and serpentinites ($R_c$ = 0.19; 1332-1493.15 m) and diopside-tremolite skarns and black schists ($R_c$ = 0.112; 1451.5-1514.3 m) can produce strong reflections as observed in the FIRE profile.
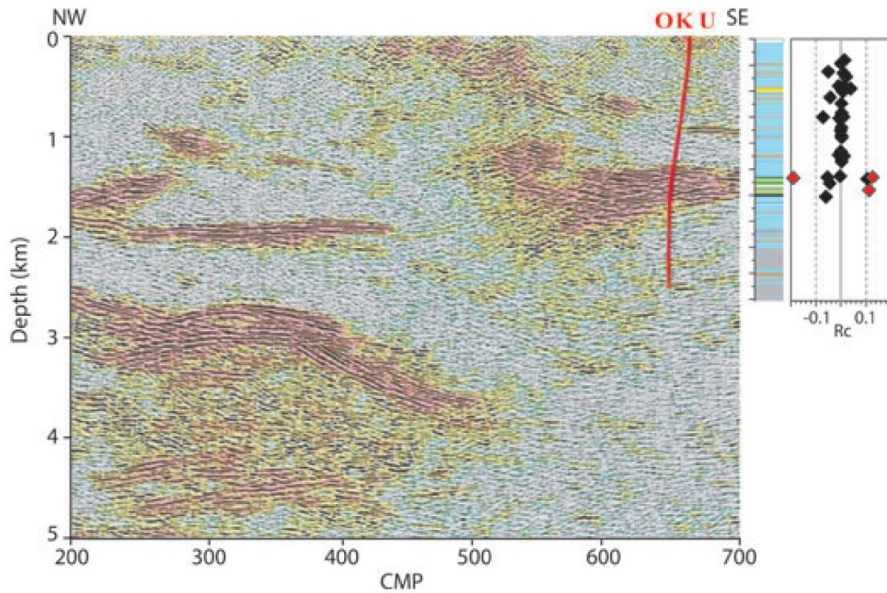


Figure 18. Left: Seismic reflection profile from FIRE 3 transect with Outokumpu deep drill core (adapted from [112]. Right: reflection coefficients (Rc) determined in this study.

Table 3. Seismic reflection coefficients for each pair of lithological units calculated based on lithology $R_c = \frac{\rho_2 V_{P2} - \rho_1 V_{P1}}{\rho_2 V_{P2} + \rho_1 V_{P1}}$. Lithological contacts that are not met in the drill core are marked as '-'.[113]

| Lithology | Mica Schist | Biotite gneiss | Chlorite-sericite schist | Black schist | Diopside-tremolite skarn | Serpentinite | Pegmatite granite |
|---|---|---|---|---|---|---|---|
| Mica schist | | -0.003 | 0.01 | 0.014 | 0.126 | - | -0.023 |
| Biotite gneiss | 0.003 | | 0.012 | - | - | - | -0.02 |
| Chlorite-sericite schist | -0.01 | - | | - | - | - | - |
| Black schist | -0.014 | - | - | | 0.112 | -0.08 | - |
| Diopside-tremolite skarn | - | - | - | -0.112 | | -0.09 | - |
| Serpentinite | - | - | - | - | 0.19 | | - |
| Pegmatite granite | 0.023 | 0.02 | - | - | - | - | |

## 4.5. Outokumpu results

The upper schist series exhibited average $Vp$ and of 5426 m/s and the ophiolitic complex 5767 m/s. With increasing pressure, the $Vp$ in the upper schist series increased slightly more than with the ophiolitic rocks. The $Vs$ values were comparable with 3051 m/s for upper schist series and 3084 m/s for ophiolitic complex at low

pressures (<10 MPa). At higher pressures (>30 MPa) the ophiolitic rocks exhibited lower $Vs$ (3135 m/s) than the schists. At 30 MPa the highest velocities in the upper schist series were recorded in the chlorite-sericite schists (5704 m/s, 3495 m/s), followed by the mica schists (5534 m/s, 3152 m/s) and the biotite gneisses (5435 m/s, 2996 m/s).

In the ophiolitic complex at 30 MPa the diopside-tremolite skarns had higher velocities (6572 m/s, 3752 m/s) than the serpentinites (5309 m/s, 2516 m/s).

The $Vp/Vs$ ratios varied from 1.6-1.85 and the calculated Poisson's ratios were 0.2-0.3 for other lithologies except for serpentinites, which exhibited $Vp/Vs$ of 2.11 and Poisson's ratio of 0.35.

The pressure dependence of the velocities, $Vp/Vs$ ratio and Poisson's ratio was monitored with water-saturated and dry samples under constant and varying temperature. Both $Vp$ and $Vs$ increase rapidly with increasing pressure, especially within the first 40 MPa. At higher pressure the velocity increase with pressure slows down.

Change in temperature (20-100°C) didn't reveal significant changes in $Vp$ whereas a decrease in $Vs$ with increasing temperature was observed at higher (≥30 MPa) pressure (Figure 20).

The $Vp$ values of dry rock samples were lower than those of water-saturated specimens.
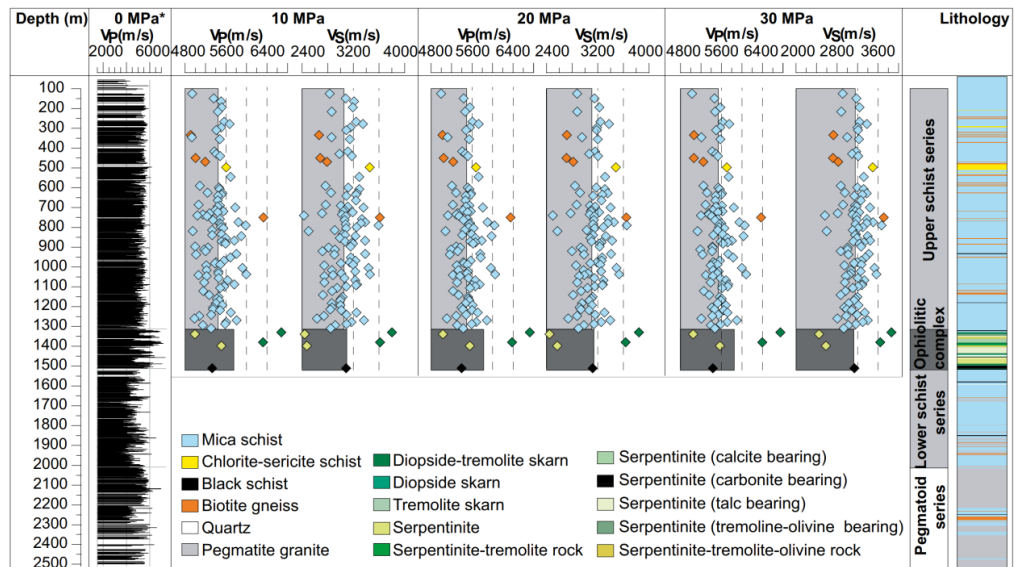


Figure 19. $Vp$ and $Vs$ of water-saturated samples at 10 MPa, 20 MPa and 30 MPa pressure. Velocity increases with increasing pressure. Separate sample data points are colored according to their lithology. The gray boxes underneath represent the average values of the series under corresponding pressure. Lithology column on the right is drawn after [113].

Table 4. Seismic velocites Vp and Vs, their ratios Vp/Vs and Poisson's ratios of water-saturated and dry rock samples under 10-40 MPa stress. On the right dry samples measured with simultaneously varying temperature (250-50°C) and stress (100-10 MPa). The properties listed under rocks are density D (g/cm³), porosity P (%), magnetic susceptibility k ($10^{-6}$ (SI convention)) and intensity of natural remanent magnetization J (mA/m). Velocity values marked with * are based on single measurements.

| Sample | Pressure MPa | Water saturated 20 °C | | | | Dry 20 °C | | | | Dry 50 °C | 140 °C | 190 °C | 250 °C |
|---|---|---|---|---|---|---|---|---|---|---|---|---|---|
| | | 10 | 20 | 30 | 40 | 10 | 20 | 30 | 40 | 10 | 50 | 75 | 100 |
| Mica schist | $V_P$ | 5423 | 5497 | 5534 | 5610 | 5178 | 5338 | 5428 | 5475 | 4545 | 5179 | 5256 | 5312 |
| D 2.74 | $V_S$ | 3051 | 3114 | 3152 | 3189 | 2947 | 3023 | 3076 | 3110 | 2713 | 2912 | 2926 | 2949 |
| P 0.53 | $V_P/V_S$ | 1.78 | 1.77 | 1.76 | 1.76 | 1.76 | 1.77 | 1.77 | 1.77 | 1.68 | 1.78 | 1.80 | 1,80 |
| k 302 | Poisson's ratio | 0.27 | 0.26 | 0.26 | 0.26 | 0.26 | 0.26 | 0.26 | 0.26 | 0.22 | 0.27 | 0.27 | 0,28 |
| J 1.99 | $Z_P$ | 1.49 | 1.51 | 1.51 | 1.57 | 1.43 | 1.46 | 1.48 | 1.48 | 1.25 | 1.42 | 1.44 | 1,46 |
| | | | | | | | | | | | | | |
| Biotite gneiss | $V_P$ | 5361 | 5414 | 5435 | 6396* | 4855* | 4967* | 5015* | | | 5193 | 5258 | |
| D 2.79 | $V_S$ | 2937 | 2973 | 2996 | 3782* | 2759* | 2814* | 2844* | | | 2978 | 2981 | |
| P 0.64 | $V_P/V_S$ | 1.83 | 1.83 | 1.82 | 1.69* | 1.76* | 1.77* | 1.76* | | | 1.74 | 1.76 | |
| k 403 | Poisson's ratio | 0.29 | 0.29 | 0.28 | 0.23* | 0.26* | 0.26* | 0.26* | | | 0.25 | 0.26 | |
| J 0.94 | $Z_P$ | 1.50 | 1.51 | 1.52 | 1.79* | 1.40* | 1.39* | 1.36* | | | 1.45 | 1.47 | |
| | | | | | | | | | | | | | |
| Chlorite-sericite schist* | $V_P$ | 5603 | 5676 | 5704 | | | | | | | | | |
| D 2.73 | $V_S$ | 3455 | 3482 | 3495 | | | | | | | | | |
| P 0.43 | $V_P/V_S$ | 1.62 | 1.63 | 1.63 | | | | | | | | | |
| k 280 | Poisson's ratio | 0.19 | 0.2 | 0.2 | | | | | | | | | |
| J 0.27* | $Z_P$ | 1.53 | 1.55 | 1.56 | | | | | | | | | |
| | | | | | | | | | | | | | |
| Black schist* | $V_P$ | 5330 | 5396 | 5432 | | 4977* | 5085* | 5143* | | | | | |
| D 2.85 | $V_S$ | 3087 | 3120 | 3138 | | 2878* | 2904* | 2918* | | | | | |
| P 0.85 | $V_P/V_S$ | 1.73 | 1.73 | 1.73 | | 1.73* | 1.75* | 1.76* | | | | | |
| k 417 | Poisson's ratio | 0.25 | 0.25 | 0.25 | | 0.25* | 0.26* | 0.26* | | | | | |
| J 538.45 | $Z_P$ | 1.52 | 1.54 | 1.55 | | 1.47* | 1.45* | 1.42* | | | | | |
| | | | | | | | | | | | | | |
| Diopside-tremolite skarn | $V_P$ | 6501 | 6554 | 6572 | | 5881* | 5971* | 6037* | 6093* | 4553 | 5338 | 5470 | |
| D 3.03 | $V_S$ | 3709 | 3738 | 3752 | | 3623* | 3656* | 3676* | 3691* | 2726 | 3076 | 3158 | |
| P 0.31 | $V_P/V_S$ | 1.75 | 1.76 | 1.75 | | 1.62* | 1.63* | 1.64* | 1.65* | 1.67 | 1.74 | 1.73 | |
| k 128 | Poisson's ratio | 0.26 | 0.26 | 0.26 | | 0.19* | 0.20* | 0.21* | 0.21* | 0.21 | 0.25 | 0.25 | |
| J 2.42 | $Z_P$ | 1.97 | 1.99 | 1.99 | | 1.85* | 1.83* | 1.811* | 1.78* | 1.38 | 1.62 | 1.66 | |
| | | | | | | | | | | | | | |
| Serpentinite | $V_P$ | 5252 | 5294 | 5309 | | | | | | 4576 | 4936 | 5173 | |
| D 2.62 | $V_S$ | 2457 | 2508 | 2516 | | | | | | 2448 | 2514 | 2598 | |
| P 3.09 | $V_P/V_S$ | 2.14 | 2.11 | 2.11 | | | | | | 1.88 | 1.97 | 2.01 | |
| k 13790 | Poisson's ratio | 0.36 | 0.35 | 0.35 | | | | | | 0.29 | 0.32 | 0.33 | |
| J 1080.48 | $Z_P$ | 1.38 | 1.39 | 1.39 | | | | | | 1.20 | 1.29 | 1.36 | |
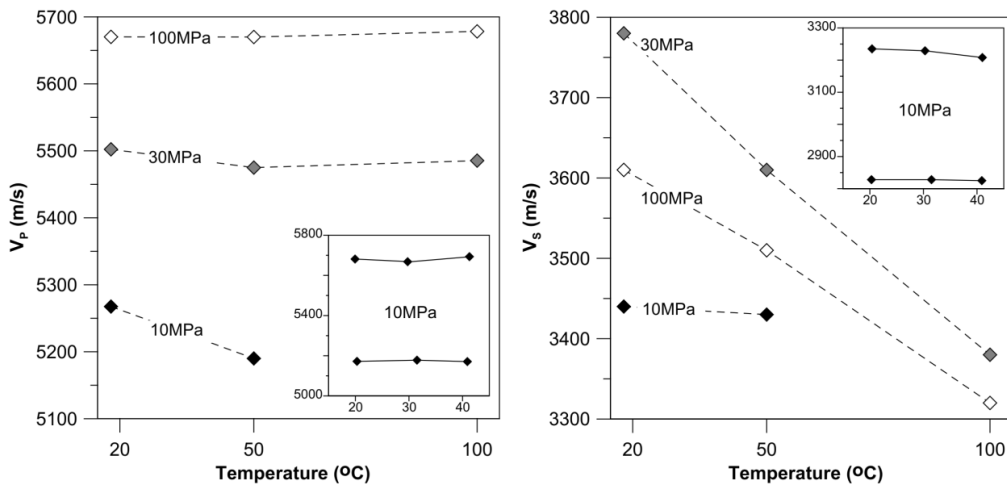


Figure 20. The temperature dependence of Vp and Vs in different mica schist samples. Vp is not affected by temperature whereas Vs decreases with increasing temperature.
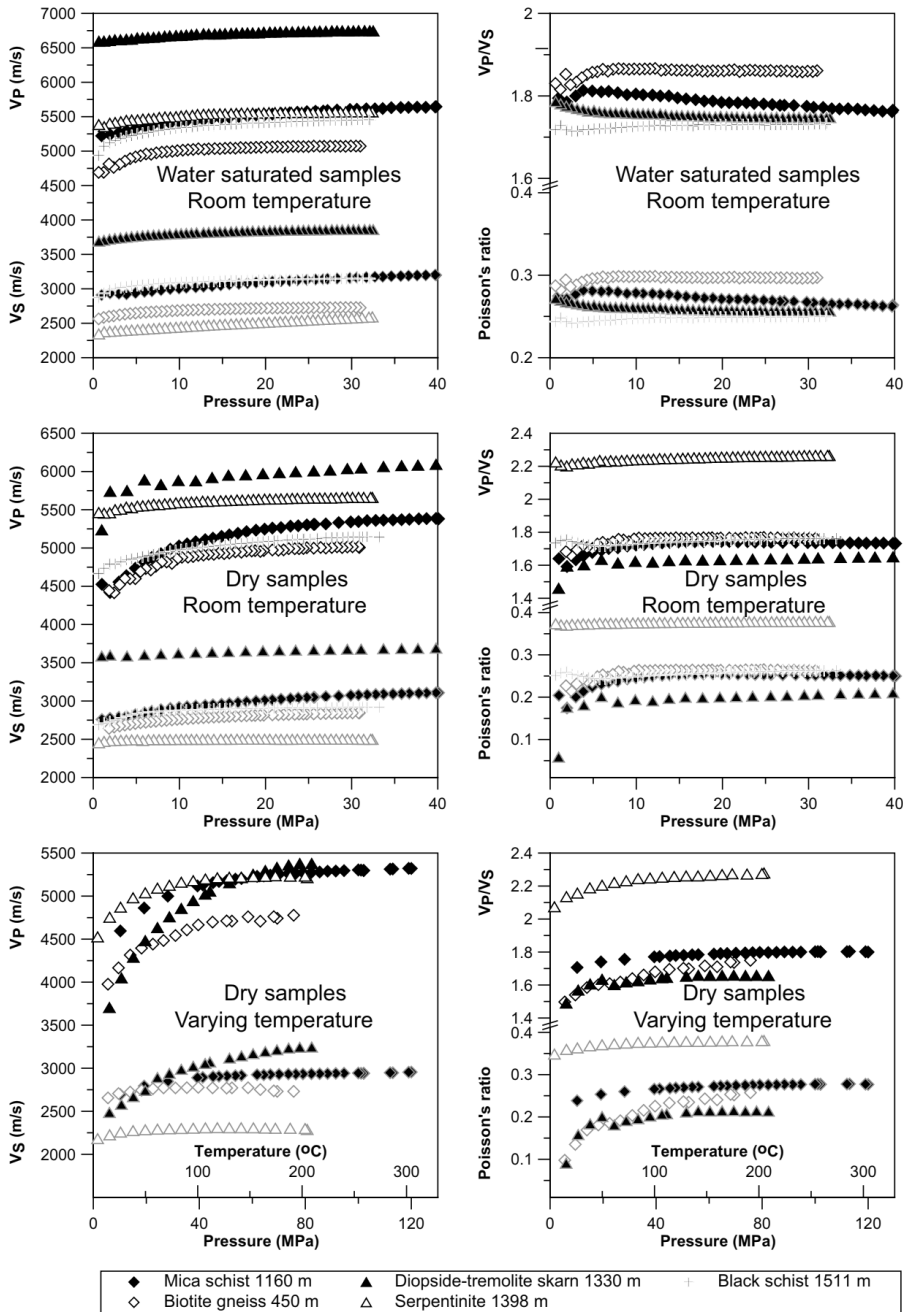
Figure 21. *Vp* and *Vs* (left column), *Vp/Vs* and Poisson's ratio (right column) of water saturated samples at room temperature (top row), dry samples at room temperature (middle row) and dry samples at varying temperature and uniaxial stress (bottom row, note different pressure range). The highest velocities were observed with diopside-tremolite skarn, lowest *Vp* with biotite gneiss and *Vs* with serpentinite. Increasing pressure had more effect on *Vp* of dry samples than for *Vs* or for water saturated samples. The *Vp/Vs* was highest for dry serpentinite and lowest for dry diopside-tremolite skarn. Water saturated mica schist and diopside-tremolite skarn featured lowering *Vp/Vs* and Poisson's ratios, whereas all the other parameters increase with pressure.

47

## 4.6. Ultrasonic velocities obtained with Triaxial setup

An example of the signals for all channels (*P*-wave, *S*-wave 0° and 90° orientations) in all directions (x, y and z) are presented in Figure 22.

For the 11 measured samples the *Vp* values varied between 3408-7250 m/s and *Vs* values 2460-4140 m/s at 2-102 MPa pressure. The gneiss and granite samples yielded lower velocities than amphibolite and diabase. The determined velocity anisotropy was 2-22% and it decreased with increasing pressure. As an example, the *Vp* and *Vs* (0° and 90° polarization) are represented in Figure 23 as a function of pressure for sample #138. For this sample the *Vp* anisotropy is more sensitive to pressure than the *Vs* anisotropies.

The *Vp* anisotropy for four representative samples is represented in Figure 24. Samples #111 diabase and #138 mica gneiss show a steeper drop in anisotropy with increasing pressure whereas samples #107 diabase and #135 even grained granite exhibit lower velocity anisotropy and are less sensitive to pressure.

The mean velocity anisotropies determined at 2 MPa and 102 MPa pressure are presented in Table 5.
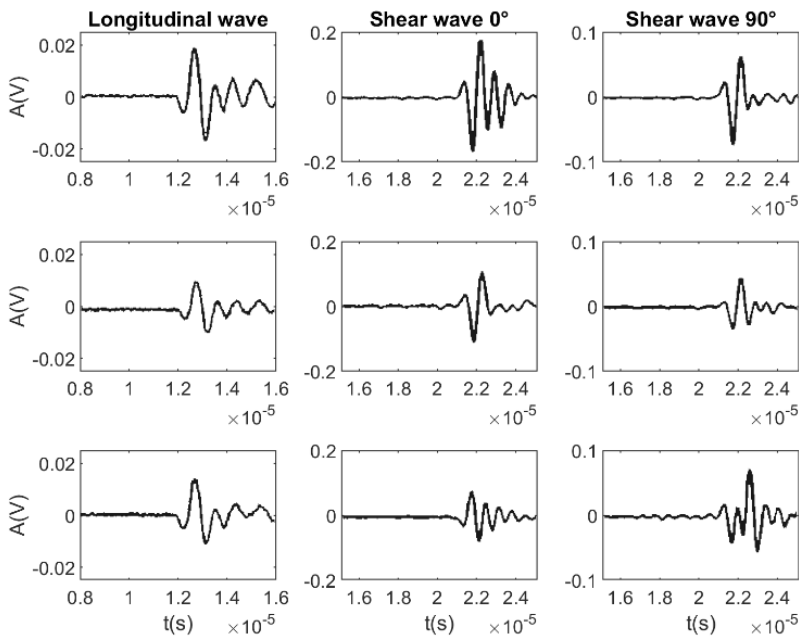


Figure 22. Ultrasonic signals through sample #135 recorded under 46 MPa pressure. The arrival time of the longitudinal signals (left column) is at ~12 µs and the shear wave signals (0° and 90° polarization in middle and right column respectively) at ~21 µs. The x-, y-, and z-directions are on first, second and third row respectively.
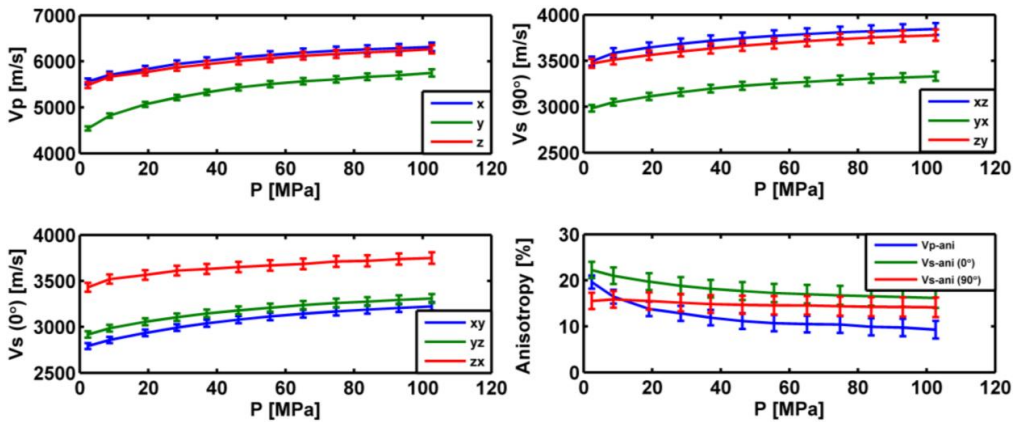
Figure 23. *Vp* (top left), *Vs* (0° bottom left, 90° top right) and velocity anisotropy (bottom right) of sample #138 in x-, y- and z-directions. All velocities increase with increasing pressure, while all anisotropies except *Vs* 90° decrease with increasing pressure.
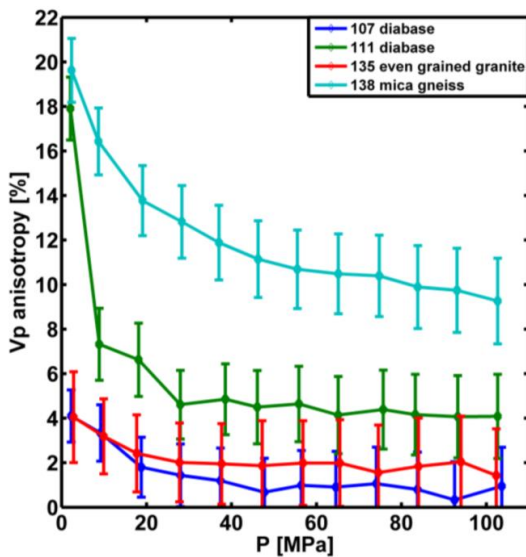


Figure 24. *Vp* anisotropy of diabase, granite and mica gneiss samples as a function of pressure. The decrease of anisotropy with increasing pressure is most notable with diabase (18-4%). The velocity anisotropy at 100 MPa is 9% for mica gneiss and <2% for diabase and granite.

Table 5. Mean $Vp$, $Vs(0°)$ and $Vs(90°)$ and standard deviations (s.d.) for rock samples from FIRE reflection seismic transects (Figure 11) determined under 2 MPa and 102 MPa triaxial pressure. Porosities $\Phi$ and densities $\rho$ are on left.

| Nr. | Sample name | φ | ρ | (2 MPa) | | | | | | | | | | | |
|---|---|---|---|---|---|---|---|---|---|---|---|---|---|---|---|
| | | | | (Vp) | s.d. | Vs (0°) | s.d. | Vs (90°) | s.d. | Ani Vp | ΔA | Ani Vs (0°) | ΔA | Ani Vs 90° | ΔA |
| | | % | kg/m³ | m/s | m/s | m/s | m/s | m/s | m/s | % | % | % | % | % | % |
| 1 | diabase | | | 4940 | 170 | 3200 | 10 | 3030 | 160 | 6.7 | 1.8 | 0.8 | 1.5 | 9.4 | 1.9 |
| 2 | granite | | | 5640 | 400 | 2990 | 180 | 3140 | 120 | 12.4 | 1.4 | 10.4 | 1.9 | 7.6 | 2.2 |
| 107 | diabase | 0.25 | 3073 | 6580 | 140 | 3860 | 40 | 3830 | 180 | 4.1 | 1.2 | 2.1 | 1.2 | 9.4 | 1.5 |
| 108 | felsic granite | 1.22 | 2605 | 4420 | 210 | 2760 | 20 | 2880 | 90 | 9.0 | 2.0 | 1.6 | 2.1 | 5.5 | 2.1 |
| 111 | diabase | 0.98 | 3050 | 5230 | 500 | 3290 | 130 | 3360 | 160 | 17.9 | 1.4 | 8.2 | 1.8 | 8.5 | 1.7 |
| 113 | amphibolite | 0.59 | 2972 | 6520 | 210 | 3800 | 150 | 3800 | 80 | 5.8 | 1.2 | 7.7 | 1.5 | 4.3 | 1.8 |
| 116 | granite gneiss | 1.25 | 2626 | 3710 | 290 | 2660 | 110 | 2590 | 80 | 15.3 | 2.0 | 8.0 | 2.2 | 5.2 | 2.3 |
| 118 | granite gneiss | 1.37 | 2685 | 4560 | 170 | 2700 | 170 | 2760 | 300 | 7.2 | 1.7 | 12.4 | 1.7 | 21.9 | 2.1 |
| 135 | even grained granite | 1.22 | 2606 | 4470 | 90 | 2810 | 50 | 2780 | 80 | 4.0 | 2.0 | 3.3 | 1.7 | 5.6 | 2.2 |
| 136 | weathered granite gneiss | 1.15 | 2655 | 4200 | 240 | 2610 | 130 | 2630 | 220 | 10.5 | 2.1 | 9.4 | 2.2 | 15.2 | 2.2 |
| 138 | mica gneiss | 0.69 | 2687 | 5190 | 570 | 3060 | 360 | 3300 | 280 | 19.6 | 1.4 | 22.2 | 1.8 | 15.5 | 1.8 |

| (102 MPa) | | | | | | | | | | | |
|---|---|---|---|---|---|---|---|---|---|---|---|
| (Vp) | s.d. | Vs (0°) | s.d. | Vs (90°) | s.d. | Ani Vp | ΔA | Ani Vs (0°) | ΔA | Ani Vs 90° | ΔA |
| m/s | m/s | m/s | m/s | m/s | m/s | % | % | % | % | % | % |
| 6580 | 540 | 3370 | 230 | 3630 | 70 | 14.5 | 1.8 | 11.7 | 2.3 | 3.7 | 2.5 |
| 6900 | 30 | 3970 | 20 | 4000 | 60 | 0.9 | 1.7 | 0.8 | 1.7 | 2.9 | 2.0 |
| 5690 | 120 | 3470 | 10 | 3510 | 30 | 4.2 | 2.3 | 0.4 | 2.0 | 1.6 | 2.3 |
| 6550 | 140 | 3800 | 80 | 3840 | 150 | 4.1 | 1.9 | 4.2 | 2.1 | 7.2 | 2.3 |
| 6770 | 330 | 3900 | 100 | 3980 | 140 | 8.9 | 1.8 | 4.6 | 2.0 | 6.5 | 2.2 |
| 5840 | 210 | 3540 | 100 | 3540 | 90 | 7.1 | 2.1 | 5.3 | 2.0 | 4.8 | 2.3 |
| 5900 | 80 | 3490 | 160 | 3600 | 40 | 2.5 | 2.1 | 8.0 | 1.9 | 1.7 | 2.2 |
| 5900 | 40 | 3560 | 0 | 3590 | 10 | 1.4 | 2.1 | 0.2 | 1.9 | 0.3 | 2.5 |
| 5820 | 110 | 3490 | 140 | 3400 | 180 | 3.9 | 2.3 | 6.9 | 2.2 | 9.3 | 2.4 |
| 6110 | 310 | 3440 | 300 | 3640 | 270 | 9.3 | 1.9 | 16.1 | 2.1 | 14.1 | 2.1 |

## 4.7. Porosity results

Figure 25 represents the correlation between ultrasound velocities and porosity in the ceramic samples. Table 6 outlines the main results. Both longitudinal and shear wave velocities decrease with increasing porosity. The highest longitudinal velocities were 4935 m/s and 4800 m/s and shear velocities 3246 m/s and 3196 m/s for saturated and dry sample (F2) respectively. For the more porous sample the lowest longitudinal velocities were 1399 m/s and 1412 m/s for saturated and dry (G1) sample respectively, whereas the lowest shear wave velocities were 1026 m/s and 1107 m/s for saturated and dry (A2) sample respectively.
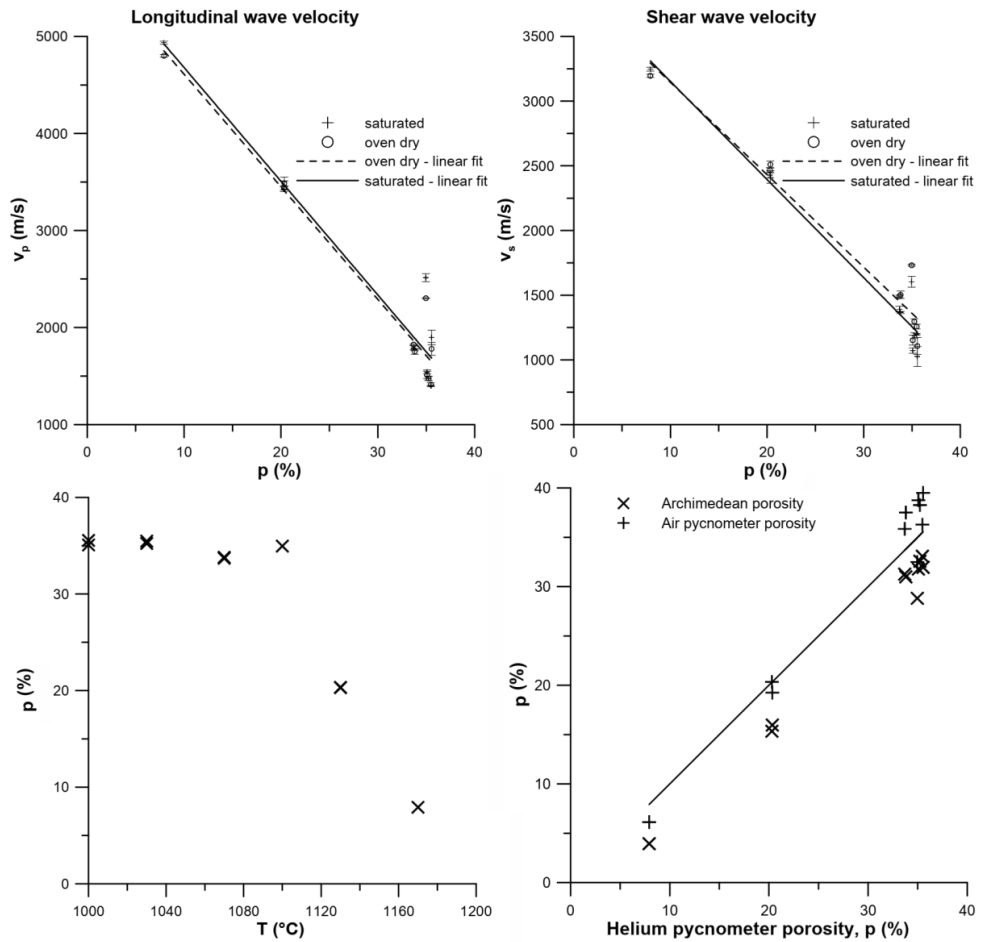
Figure 25. Correlation between *Vp* (top left) and *Vs* (top right) and porosity derived from helium gas pycnometry for dry and water saturated ceramic samples. The relation between the baking temperature and porosity (determined with helium pycnometer) shows that 1100-1170°C temperature range produced varying porosity (bottom left). Porosities determined by Archimedean method and air pycnometry are compared to helium pycnometry. Archimedean method yields lower values than air pycnometry while they both exhibit lower porosity values compared to helium pycnometry (bottom right).

Table 6. Sample firing temperature (*T*), bulk (*D_B*) and grain (*D_G*) densities, porosity (*p*) determined by Archimedean method (average of three measurements, F2, G1 and G2 average of two measurements), air and helium pycnometry, *Vp*, and *Vs* for water saturated and dry samples. Bulk density was calculated from mass and sample geometry. Grain density was calculated from mass and grain volume determined by helium pycnometer.

| Sample | T (°C) | He. pyc. DG (kg/m³) | Geom. DB (kg/m³) | Arch. p (%) | Air pyc. p (%) | He pyc. p (%) | Saturated $v_p$ (m/s) | Saturated $v_s$ (m/s) | Oven dry $v_p$ (m/s) | Oven dry $v_s$ (m/s) |
|---|---|---|---|---|---|---|---|---|---|---|
| A1 | 1000 | 2635 | 1698 | 32 | 39 | 36 | 1898 | 1026 | 1781 | 1107 |
| A2 | 1000 | 2637 | 1712 | 32 | 39 | 35 | 1542 | 1072 | 1512 | 1152 |
| G1 | 1030 | 2625 | 1694 | 33 | 36 | 36 | 1399 | 1198 | 1412 | 1257 |
| G2 | 1030 | 2633 | 1705 | 33 | 38 | 35 | 1477 | 1188 | 1476 | 1296 |
| B1 | 1070 | 2621 | 1735 | 31 | 38 | 34 | 1769 | 1366 | 1753 | 1503 |
| B2 | 1070 | 2621 | 1738 | 31 | 36 | 34 | 1790 | 1392 | 1825 | 1493 |
| E1 | 1100 | 2608 | 1696 | 29 | 32 | 35 | 2514 | 1603 | 2302 | 1731 |
| C1 | 1130 | 2579 | 2055 | 16 | 19 | 20 | 3503 | 2413 | 3484 | 2510 |
| C2 | 1130 | 2572 | 2050 | 15 | 20 | 20 | 3424 | 2428 | 3437 | 2466 |
| F2 | 1170 | 2453 | 2259 | 4 | 6 | 8 | 4935 | 3246 | 4800 | 3196 |

## 4.8. Ultrasound-initiated nucleation

The crystal growth kinetics was studied by collecting samples during the process from which the particle size distribution (PSD) was then determined (Figure 26). The PSD was also determined from the end-product (Figure 27). The mode of the distribution described the average crystal size. A comparison of the smallest size fractions obtained during the process to the PSDs of the end products revealed that sonication increases the nucleation rate whereas the nucleation rates are lowest in the case of seeding. Sonication reduced the crystal size in the end-product. The longer sonication time (11 min) produced smaller crystals (mode 35 µm) than shorter sonication time (1 min) and the largest particles (mode 120 µm) were produced without sonication.

Seeding increased the crystal size slightly compared to spontaneous nucleation. The mode of the distribution was 130 µm and 120 µm for the crystals produced using seeding and spontaneous nucleation, respectively. This can be also observed from the SEM images (Figure 28).

The set pre-nucleation supersaturation values of 1 M produced more of $\alpha$-polymorph than $\beta$-polymorph whereas the 0.7 M supersaturation produced mostly $\beta$-polymorph (Figure 29). The highest fraction of $\alpha$-polymorph (>99.5%) resulted from the longest sonication time. Sonication didn't affect the polymorph at the 0.7 M supersaturation but did yield in smaller particle size (Figure 27, Figure 28).
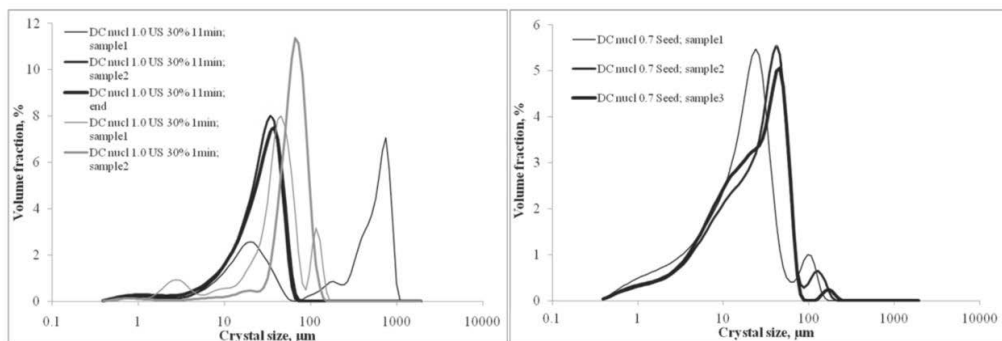
Figure 26. PSDs were determined from samples collected during the process to study the crystal growth kinetics. On left: 1 M supersaturation to produce α-polymorph using sonication. With 11 min sonication time "sample 1" was collected at 6 min (the bimodal distribution was possibly caused by aggregation.), "sample 2" at 16 min "sample end" at 22 min. With 1 min sonication time "sample1" was collected at 5 min and "sample2" at 12 min. On right: 0.7 M supersaturation to produce β-polymorph with seeding. Samples 1, 2 and 3 were collected at 13 min, 24 min and 34 min, respectively.
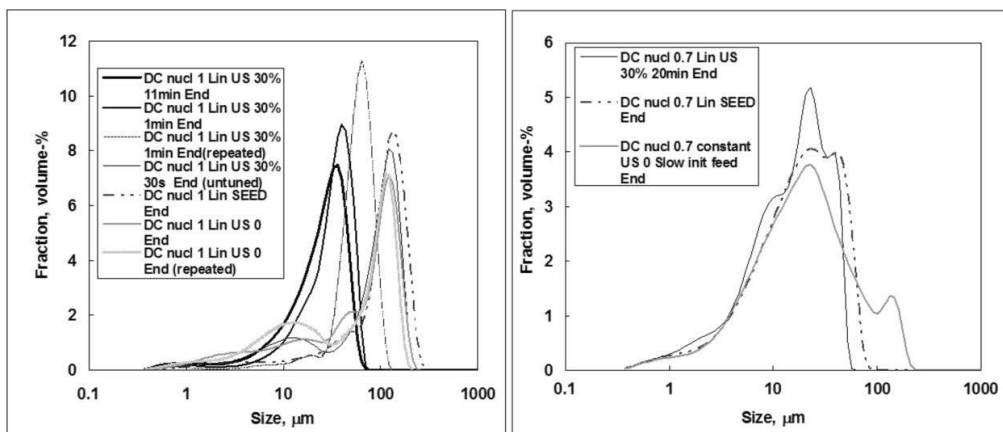


Figure 27. Particle size distributions of crystal samples obtained after the batch process. Left: 1 M supersaturation to produce α-polymorph. Right: 0.7 M supersaturation to produce β-polymorph: In both cases, sonication reduced the particle size compared to seeded and spontaneously nucleated batches.

1M, US 30% 11 min         1 M, US 30% 1 min         1 M, US untuned 0.5 min

1 M, Seed              1 M, US 0%              1 M, US 0%

0.7 M, US 30% 20 min       0.7 M Seed           0.7 M, US 0%
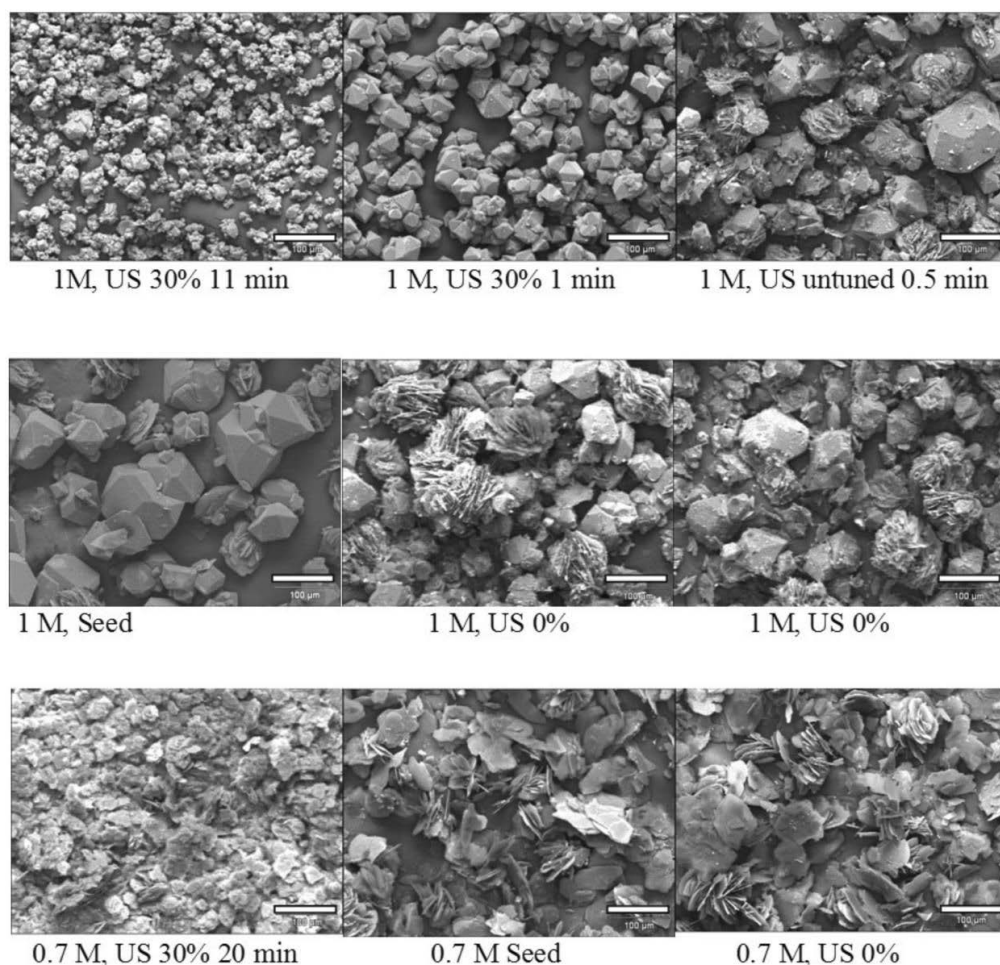
Figure 28. SEM images of *L*-glutamic acid crystals. Sonication (top row) produced pure *α*-polymorph (unstable, prismatic or granular shaped). Increasing sonication time decreased particle size. Seeding (middle row, left) produced also mostly *α*-polymorph while the particle size was larger. Spontaneously formed crystals (middle row, middle and right) in same supersaturation (1 M) included both *α*- and *β* -polymorph. The 0.7 M supersaturation produced pure *β*-polymorph (stable, needle or flake shaped) (bottom row). Sonication reduced the particle size (bottom row, left) compared to spontaneous nucleation (bottom row, middle and right).

Figure 29. Mass fraction of the *α*-polymorph of *L*-glutamic acid determined by Raman spectroscopy. Left (1 M supersaturation): The *α*-polymorph fraction reached the maximum value in sonicated and seeded batches right after nucleation phase. The spontaneous crystallizations show variation in *α*-polymorph fraction during process. Even the untuned 30 s sonication increased the *α*-polymorph fraction. Right (0.7 M supersaturation): 10% *α*-polymorph fraction was observed at nucleation phase in the s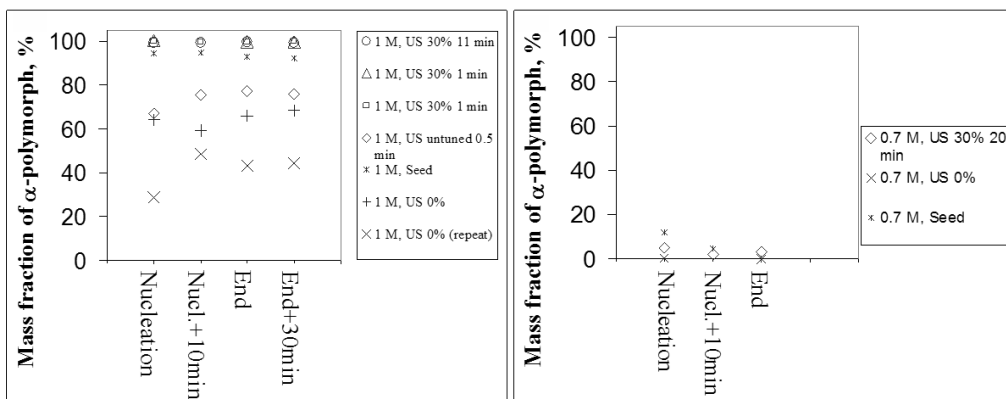eeded batch after which mainly *β*-polymorph was observed. Sonicated and spontaneously crystallized batches featured mainly *β*-polymorph throughout the experiments.

# 5. DISCUSSION

## 5.1. Observations from uniaxial configuration

The built apparatus employing uniaxial compression produced similar *Vp* and *Vs* results as multi-anvil apparatus for drill core rock samples under 5-300 MPa compression with some differences. The well-known nonlinear increase in velocity is caused by progressive closure of microcracks, illustrating the pressure sensitivity of *Vp* and *Vs*. The following linear region reflects the intrinsic properties of the compacted rock, such as the composition of minerals, elastic properties of single crystals and their crystallographic preferred orientation [77], [114], [115].

The *Vp* at low pressure is higher in the uniaxial case compared to the multi-anvil results. This could be due to horizontal microcracks closing more readily under uniaxial stress. At high pressure, the *Vp* values match closely showing that the cracks have been closed. Contrarily, *Vs* under uniaxial compression is slightly lower at all pressures compared to multi-anvil results. This could be due to vertically aligned cracks closing more readily in a multi-anvil device. Also the change in the elastic constants of matrix material from the increased contact stiffness between particles under confining pressure might have similar effect [60].

The *Vp* increased slightly more than *Vs* with increasing uniaxial stress. This is likely related to foliation, microcracks and resulting elastic anisotropy [60], [114].

Outokumpu core samples have been reported to exhibit strong elastic anisotropy. It is largely caused by crystallographic preferred orientation, alignment of platy minerals

and oriented microcracks. Because of these effects the velocities in horizontal directions are higher than in vertical direction [10]. The velocity measurements with the uniaxial apparatus were conducted normal to the foliation plane in vertical (along the core) direction. Thus, the results give the minimum values of the possible velocities.

The measured samples that were used in comparison were mica schist. In a study [92], the uppermost 2 km of the drill hole was considered "mainly mica schist with minor biotite gneiss, chlorite-sericite schist, black schist and hornblende-epidote schist intercalations". In the reference study [10] the samples from same depth were labeled biotite gneiss. Biotite gneiss (mica schist) was referred there as the dominating rock species in the crustal section. From ultrasonic point of view, the samples were assumed sufficiently similar, to make the comparison relevant.

In the uniaxial measurement configuration, the sample support ring is required to prevent the sample rock from cracking under stress. As the sample compresses under axial stress it expands in the radial direction, governed by the Poisson's ratio of the material. The support ring prevents the expansion and the configuration essentially turns into (non-true) triaxial configuration. The sample diameter was uniform within the sample sets. Variation in diameter would have changed the radial support. The radial support could be measured by equipping the support ring with circumferential strain gage. Developing the method further, the next step would be to equip the device with a system to control the radial stress.

FEM simulations were used to describe the stress state inside the sample under compression. The contact between the sample, holder and transducers is somewhere between sliding and bonded. Compared to the situation without the sample holder, the axial stress can be 10% smaller while the radial and tangential stress components can be more than 10% of the axial stress value in case of 0.5 friction coefficient.

The sample height was measured with a caliper with Vernier scale resolution of 0.05 mm. In practice, the estimated accuracy of the height measurement was 0.1 mm due to surface roughness and deviations in parallelism of the sample surfaces. The estimated error in the time of flight from the averaged, interpolated signal was 2 ns, in case of non-dispersive sample. The error in the calculated velocity was estimated as 20 m/s with propagation of uncertainty.

Water saturated upper gneiss series samples from Outokumpu hole exhibited 8% higher *Vp* values at 30 MPa measured with uniaxial apparatus compared to dry samples measured with multi-anvil [10]. The effect of water saturation on *Vp* is well known [116]. Water saturation did not have noticeable effect on *Vs*.

The upper schist series features velocity variations. Some of them arise from the lithological differences but there are also velocity fluctuations within the same lithology. Velocities are especially sensitive to microfracturing. The possible mechanisms for microfracturing are: (1) microcracks in *in-situ* rocks, (2) drilling induced microcracks and (3) fracturing due to the stress release during the extraction of the core. The stress release induced fracturing is supported by the observation that the velocity decreases with increasing depth for samples measured under ambient

pressure conditions and the velocity increases during loading when microcracks are supposed to close (Figure 17). It is also reported that oriented microcracks allow discriminating between core samples and surface rocks [117]. The closing pressure showed little variation, which implies that the crack density was similar between the samples. Low crack density results in low microcrack closing pressure (50-80 MPa), whereas densely cracked samples have been reported to close at higher pressure (150-200 MPa) [118].

It should be noted that the pressure corresponding to the sample depth does not completely close the stress release induced microcracks [10]. Thus, the represented core sample velocities are lower than the seismic velocities in crust. The closing of the cracks can be observed at ~50 MPa pressure when the velocity increase with increasing pressure starts to decrease. This should be noted in all laboratory velocity measurements of rock samples.

## 5.2. Observations from multi-anvil configuration

The velocity anisotropies in the FIRE samples at low pressure were up to 22±2%. The anisotropy decreased with increasing pressure with most samples, most likely because of closing of microcracks. The measurements showed that the velocity anisotropy in Fennoscandian shield is significant and should be accounted in interpretation of seismic data. This agreed with previous studies [10].

The multi-anvil has three fixed transducers and three transducers that move during the compression. During the sample compression there is friction between the transducers and the compressed sample. Because three transducers are fixed, and three transducers move with the compression the shear stress is not symmetrical on the sample surfaces. Symmetric shear stress would result from equal compression from all sides, that would require six hydraulic cylinders.

The transducer faces are smaller than the sample faces to allow sample size variation and sample compression. The transducers do not produce stress on the corners of the sample, which can lead to non-uniform stress distribution. Because the first arriving signal probes the volume straight ahead from transducer front face, effect on measured velocities is small.

To mimic the crustal conditions more precisely the loading of the sample should be done independently for all axis. This would require a separate control valve for each cylinder. Also, the loading would need to be monitored in three directions.

## 5.3. Observations from porosity measurement

Empirical relation between *Vp* and *Vs* and porosity in compositionally similar ceramic samples was confirmed. The results met the expectations and were consistent with previous studies [71], [72]. Velocity decreased linearly (RMS 0.93-0.96) with increasing porosity until 33% porosity.

This was expected as the velocity in the fluid filling the pores is slower than in the matrix material. There is a slight increase in *Vp* with water saturated samples compared to dry samples. This is because *Vp* in water is higher (1480 m/s) than in air (343 m/s) [24]. *Vs* showed the opposite trend, which derives from increased density while the shear modulus is not influenced [27].

In case of water saturated samples, it is expected that the measured velocity will approach the sound velocity in water with increasing porosity. Dry samples exhibited the same behavior, but also nearly same velocity, which points to different mechanism.

Helium pycnometer measurements were used as reference values. Compared to Archimedean water immersion method, gas pycnometry probes a larger volume of the sample. The helium atoms are smaller than $H_2O$ molecules and can reach smaller pores. Still, the gas pycnometer is only sensitive to interconnected pores.

## 5.4. Observations from sonocrystallization

A 1 M supersaturation was used to produce the metastable $\alpha$-polymorph and prevent the formation of the stable $\beta$-polymorph. The crystal size was reduced with prolonged sonication time (11 min). The PSD was narrower for sonicated samples compared to non-sonicated samples. The small particle size and narrow PSD were caused because sonication induced nucleation and more nuclei were formed at once. This allowed the particles to grow together as one population. The saturation level quickly decreased, and no further nucleation happened outside the sonication region.

The PSDs from the two experiments with 1 min sonication times were not identical. Nevertheless 1 min sonication time ensured the production of pure $\alpha$-polymorph. The different PSDs could have resulted from slight changes in the supersaturation. Even a sonication that was interrupted after 30 s increased the $\alpha$-polymorph concentration compared to non-sonicated experiments.

Seeding produced >90% pure $\alpha$-polymorph. It was speculated that the small $\beta$-polymorph fraction resulted because the growth rate of the $\beta$-polymorph exceeded the seeding induced secondary nucleation and resulting $\alpha$-polymorph growth rate [119].

In case of 0.7 M supersaturation, sonication or seeding did not have significant effect on $\alpha$-polymorph concentration, since the $\beta$-polymorph formation dominates under these conditions. Different polymorphs exhibit different solubilities and thus their prevalence in a solution can be controlled by the supersaturation level.

# 6. CONCLUSIONS

A device for measuring ultrasonic velocities of rock core samples under uniaxial loading was built. The uniaxial measurement apparatus allowed to determine *Vp* and *Vs* values requiring minimal sample preparation compared to multi-anvil technique

with comparable results. The stress state under uniaxial compression differs from that in a multi-anvil, which affects the sound propagation and needs to be considered when comparing the results. In case the samples exhibit velocity anisotropy the usability of the method is limited because the velocity is measured only in one direction.

The seismic reflection coefficients for different lithologies in the Outokumpu drill hole were estimated. The strong reflectors observed in the FIRE reflection data were identified as contacts of diopside -tremolite skarn into serpentinites, into black schist or into mica schist.

With anisotropic rocks, it is beneficial to perform the velocity measurements using a multi-anvil apparatus. An apparatus was built in which *Vp* and *Vs* (0° and 90° polarization) were measured in three orthogonal directions during single loading cycle. For more realistic reproduction of crustal conditions, the multi-anvil axes should be controlled separately.

An empirical relation between velocities and porosity in a range of 4-33% was found in compositionally similar ceramic samples.

Sonication was used to control the polymorphism and crystal size of *L*-glutamic acid at suitable supersaturation level.

# REFERENCES

[1] K. C. Condie, 'Chapter 2 - The Crust', in *Earth as an Evolving Planetary System (Second Edition)*, K. C. Condie, Ed. Boston: Academic Press, 2011, pp. 11–58.

[2] W. Lowrie, *Fundamentals of Geophysics*, 2nd edition. Cambridge; New York: Cambridge University Press, 2007.

[3] R. Meissner, J. Marshall, and R. A. Plumb, *The Continental Crust: A Geophysical Approach*. Academic Press, 1986.

[4] N. I. Christensen and W. D. Mooney, 'Seismic velocity structure and composition of the continental crust: A global view', *J. Geophys. Res. Solid Earth*, vol. 100, no. B6, pp. 9761–9788, 1995.

[5] W. L. Russell, *Structural Geology for Petroleum Geologists;* 1955, 1955.

[6] H. Berckhemer *et al.*, 'Petrophysical properties of the 9-km-deep crustal section at KTB', *J. Geophys. Res. Solid Earth*, vol. 102, no. B8, pp. 18337–18361, 1997, doi: 10.1029/96JB03396.

[7] I. T. Kukkonen, *Outokumpu Deep Drilling Project 2003 - 2010*. Geological Survey of Finland, 2011.

[8] B. Beránek and V. Tobyáš, 'Study of the velocity conditions in the earth's crust in the regions of the Bohemian massif and the carpathian system along international profiles VI and VII', *Stud. Geophys. Geod.*, vol. 15, no. 3, pp. 316–330, Sep. 1971, doi: 10.1007/BF01589248.

[9] I. Kukkonen and R. Lahtinen, 'Finnish Reflection Experiment FIRE 2001-2005', *Geol. Surv. Finl.*, vol. 43, Jan. 2006.

[10] H. Kern, K. Mengel, K. Strauss, T. Ivankina, A. Nikitin, and I. Kukkonen, 'Elastic wave velocities, chemistry and modal mineralogy of crustal rocks sampled by the Outokumpu Scientific Drill Hole: evidence from lab measurements and modeling', *Phys. Earth Planet. Inter. - PHYS EARTH PLANET Inter.*, vol. 175, pp. 151–166, Jul. 2009, doi: 10.1016/j.pepi.2009.03.009.

[11] S. Ji, Q. Gu, and B. Xia, 'Porosity dependence of mechanical properties of solid materials', *J. Mater. Sci.*, vol. 41, no. 6, pp. 1757–1768, Mar. 2006, doi: 10.1007/s10853-006-2871-9.

[12] R. Wheaton, 'Chapter 2 - Basic Rock and Fluid Properties', in *Fundamentals of Applied Reservoir Engineering*, R. Wheaton, Ed. Gulf Professional Publishing, 2016, pp. 5–57.

[13] L. M. Anovitz and D. R. Cole, 'Characterization and Analysis of Porosity and Pore Structures', *Rev. Mineral. Geochem.*, vol. 80, no. 1, pp. 61–164, Jan. 2015, doi: 10.2138/rmg.2015.80.04.

[14] M. Asmani, C. Kermel, A. Leriche, and M. Ourak, 'Influence of porosity on Young's modulus and Poisson's ratio in alumina ceramics', *J. Eur. Ceram. Soc.*, vol. 21, no. 8, pp. 1081–1086, Aug. 2001, doi: 10.1016/S0955-2219(00)00314-9.

[15] M. H. Anders, S. E. Laubach, and C. H. Scholz, 'Microfractures: A review', *J. Struct. Geol.*, vol. 69, pp. 377–394, Dec. 2014, doi: 10.1016/j.jsg.2014.05.011.

[16] R. L. Kranz, 'Microcracks in rocks: A review', *Tectonophysics*, vol. 100, no. 1, pp. 449–480, Dec. 1983, doi: 10.1016/0040-1951(83)90198-1.

[17] A. Holden and P. Morrison, *Crystals and Crystal Growing*, 1st MIT edition. Cambridge, Mass: The MIT Press, 1982.

[18] H. N. Kim and K. S. Suslick, 'The Effects of Ultrasound on Crystals: Sonocrystallization and Sonofragmentation', *Crystals*, vol. 8, no. 7, p. 280, Jul. 2018, doi: 10.3390/cryst8070280.

[19] D. Z. Shende, 'Reactive crystallization in pharma industry', presented at the International Conference on Pharmacognosy, Phytochemistry & Natural Products, Radisson Blu Plaza Hotel, Hyderabad, India, Oct. 2013, Accessed: Dec. 21, 2019. [Online].

[20] R. Prasad and S. V. Dalvi, 'Sonocrystallization: Monitoring and controlling crystallization using ultrasound', *Chem. Eng. Sci.*, vol. 226, p. 115911, Nov. 2020, doi: 10.1016/j.ces.2020.115911.

[21] R. Censi and P. Di Martino, 'Polymorph Impact on the Bioavailability and Stability of Poorly Soluble Drugs', *Molecules*, vol. 20, no. 10, pp. 18759–18776, Oct. 2015, doi: 10.3390/molecules201018759.

[22] R. Karlqvist, I. Lassila, E. Haeggstrom, and L. J. Pesonen, 'Anisotropy of longitudinal and shear wave velocities in rocks under controlled pressure', in *2013 IEEE International Ultrasonics Symposium (IUS)*, 2013, pp. 1575–1578, doi: 10.1109/ULTSYM.2013.0402.

[23] D. Ensminger and L. J. Bond, *Ultrasonics: Fundamentals, Technologies, and Applications, Third Edition*. CRC Press, 2011.

[24] G. S. Kino, *Acoustic Waves: Devices, Imaging, and Analog Signal Processing*. Prentice-Hall, 1987.

[25] J. L. Rose, *Ultrasonic Waves in Solid Media*. Cambridge: Cambridge University Press, 2004.

[26] C. Chapman, *Fundamentals of Seismic Wave Propagation*. 2004.

[27] S. J. Schön, 'Elastic Properties', in *Handbook of Petroleum Exploration and Production*, vol. 8, Elsevier, 2011, pp. 149–243.

[28] B. Goodway, 'AVO and Lame constants for rock parameterization and fluid detection', *Recorder*, vol. 26, no. 6, pp. 39–60, 2001.

[29] G. Mavko, T. Mukerji, and J. Dvorkin, *The Rock Physics Handbook: Tools for Seismic Analysis of Porous Media*, 2nd ed. 2009.

[30] L. E. Kinsler, A. R. Frey, A. B. Coppens, and J. V. Sanders, *Fundamentals of Acoustics*, 4th edition. New York: Wiley, 1999.

[31] L. L. Beranek, *Acoustics*. American Inst. of Physics, 1986.

[32] J. Jaeger, N. Cook, and R. Zimmerman, 'Fundamental of Rock Mechanics', 2007.

[33] J. H. Schön, *Physical Properties of Rocks: Fundamentals and Principles of Petrophysics*. Elsevier, 2015.

[34] K. Zoeppritz, 'VII b. Über Reflexion und Durchgang seismischer Wellen durch Unstetigkeitsflächen', *Nachricten Von K. Ges. Wiss. Zu Gött. Math.-Phys. Kl.*, vol. 66, 1919.

[35] W. Cheng, J. Ba, L.-Y. Fu, and M. Lebedev, 'Wave-velocity dispersion and rock microstructure', *J. Pet. Sci. Eng.*, vol. 183, p. 106466, Dec. 2019, doi: 10.1016/j.petrol.2019.106466.

[36] Y. Guéguen and J. Sarout, 'Characteristics of anisotropy and dispersion in cracked medium', *Tectonophysics*, vol. 503, no. 1, pp. 165–172, Apr. 2011, doi: 10.1016/j.tecto.2010.09.021.

[37] S. Lozovyi and A. Bauer, 'Velocity dispersion in rocks: A laboratory technique for direct measurement of P-wave modulus at seismic frequencies', *Rev. Sci. Instrum.*, vol. 90, no. 2, p. 024501, Feb. 2019, doi: 10.1063/1.5026969.

[38] G. Valsamos, F. Casadei, and G. Solomos, 'A numerical study of wave dispersion curves in cylindrical rods with circular cross-section', *Appl. Comput. Mech.*, vol.

7, no. 1, May 2013, Accessed: Jan. 12, 2020. [Online]. Available: https://www.kme.zcu.cz/acm/acm/article/view/200.

[39] L. Y. Tu, J. N. Brennan, and J. A. Sauer, 'Dispersion of Ultrasonic Pulse Velocity in Cylindrical Rods', *J. Acoust. Soc. Am.*, vol. 27, no. 3, pp. 550–555, May 1955, doi: 10.1121/1.1907961.

[40] J. B. Walsh, 'The effect of cracks on the compressibility of rock', *J. Geophys. Res. 1896-1977*, vol. 70, no. 2, pp. 381–389, 1965, doi: 10.1029/JZ070i002p00381.

[41] G. Simmons and W. F. Brace, 'Comparison of static and dynamic measurements of compressibility of rocks', *J. Geophys. Res. 1896-1977*, vol. 70, no. 22, pp. 5649–5656, 1965, doi: 10.1029/JZ070i022p05649.

[42] C. M. Sayers, 'Stress-induced ultrasonic wave velocity anisotropy in fractured rock', *Ultrasonics*, vol. 26, no. 6, pp. 311–317, Nov. 1988, doi: 10.1016/0041-624X(88)90028-5.

[43] Y. Guéguen and V. Palciauskas, *Introduction to the Physics of Rocks*. Princeton University Press, 1994.

[44] Y. Guéguen and A. Schubnel, 'Elastic wave velocities and permeability of cracked rocks', *Tectonophysics*, vol. 370, no. 1, pp. 163–176, Jul. 2003, doi: 10.1016/S0040-1951(03)00184-7.

[45] A. Schubnel, P. M. Benson, B. D. Thompson, J. F. Hazzard, and R. P. Young, 'Quantifying Damage, Saturation and Anisotropy in Cracked Rocks by Inverting Elastic Wave Velocities', *Pure Appl. Geophys.*, vol. 163, no. 5, pp. 947–973, Jun. 2006, doi: 10.1007/s00024-006-0061-y.

[46] Y. Guéguen and M. Kachanov, 'Effective Elastic Properties of Cracked Rocks — An Overview', in *Mechanics of Crustal Rocks*, Y. M. Leroy and F. K. Lehner, Eds. Vienna: Springer, 2011, pp. 73–125.

[47] M. Kachanov, 'Effective Elastic Properties of Cracked Solids: Critical Review of Some Basic Concepts', *Appl. Mech. Rev.*, vol. 45, no. 8, pp. 304–335, Aug. 1992, doi: 10.1115/1.3119761.

[48] W. Voigt, *Lehrbuch Der Kristallphysik*. Johnson Reprint Corporation, 1928.

[49] A. Reuss, 'Berechnung der Fließgrenze von Mischkristallen auf Grund der Plastizitätsbedingung für Einkristalle .', *ZAMM - J. Appl. Math. Mech. Z. Für Angew. Math. Mech.*, vol. 9, no. 1, pp. 49–58, 1929, doi: 10.1002/zamm.19290090104.

[50] R. Hill, 'The Elastic Behaviour of a Crystalline Aggregate', *Proc. Phys. Soc. Sect. A*, vol. 65, no. 5, pp. 349–354, May 1952, doi: 10.1088/0370-1298/65/5/307.

[51] Z. Hashin and S. Shtrikman, 'A variational approach to the theory of the elastic behaviour of multiphase materials', *J. Mech. Phys. Solids*, vol. 11, no. 2, pp. 127–140, Mar. 1963, doi: 10.1016/0022-5096(63)90060-7.

[52] J. R. Bristow, 'Microcracks, and the static and dynamic elastic constants of annealed and heavily cold-worked metals', *Br. J. Appl. Phys.*, vol. 11, no. 2, pp. 81–85, Feb. 1960, doi: 10.1088/0508-3443/11/2/309.

[53] C. H. Cheng, 'Crack models for a transversely isotropic medium', *J. Geophys. Res. Solid Earth*, vol. 98, no. B1, pp. 675–684, 1993, doi: 10.1029/92JB02118.

[54] Y.-G. Li, *Rock Anisotropy, Fracture and Earthquake Assessment*. Berlin/Boston, GERMANY: De Gruyter, Inc., 2016.

[55] G. Barla, 'Rock Anisotropy - Theory and Laboratory Testing', in *Rock Mechanics*, 1974, pp. 131–169.

[56] D. S. Hughes and J. H. Cross, 'Elastic wave velocities in rocks at high pressures and temperatures', *Geophysics*, vol. 16, no. 4, pp. 577–593, Oct. 1951, doi: 10.1190/1.1437706.

[57] J. W. Spencer and A. M. Nur, 'The effects of pressure, temperature, and pore water on velocities in westerly granite', *J. Geophys. Res. 1896-1977*, vol. 81, no. 5, pp. 899–904, 1976, doi: 10.1029/JB081i005p00899.

[58] H. Kern, 'The effect of high temperature and high confining pressure on compressional wave velocities in quartz-bearing and quartz-free igneous and metamorphic rocks', *Tectonophysics*, vol. 44, no. 1, pp. 185–203, Jan. 1978, doi: 10.1016/0040-1951(78)90070-7.

[59] R. Punturo, H. Kern, R. Cirrincione, P. Mazzoleni, and A. Pezzino, 'P- and S-wave velocities and densities in silicate and calcite rocks from the Peloritani Mountains, Sicily (Italy): The effect of pressure, temperature and the direction of wave propagation', *Tectonophysics*, vol. 409, no. 1, pp. 55–72, Nov. 2005, doi: 10.1016/j.tecto.2005.08.006.

[60] O. Nishizawa and K. Kanagawa, 'Seismic velocity anisotropy of phyllosilicate-rich rocks: characteristics inferred from experimental and crack-model studies of biotite-rich schist', *Geophys. J. Int.*, vol. 182, no. 1, pp. 375–388, Jul. 2010, doi: 10.1111/j.1365-246X.2010.04614.x.

[61] M. S. King, 'Wave velocities in rocks as a function of change in overburden pressure and pore fluid saturants', *Geophysics*, vol. 31, no. 1, pp. 50–73, Feb. 1966, doi: 10.1190/1.1439763.

[62] N. I. Christensen and H. F. Wang, 'The Influence of pore pressure and confining pressure on dynamic elastic properties of Berea sandstone', 1985, doi: 10.1190/1.1441910.

[63] M. Prasad and M. H. Manghnani, 'Effects of pore and differential pressure on compressional wave velocity and quality factor in Berea and Michigan sandstones', *GEOPHYSICS*, vol. 62, no. 4, pp. 1163–1176, Jul. 1997, doi: 10.1190/1.1444217.

[64] B. Scheu, H. Kern, O. Spieler, and D. B. Dingwell, 'Temperature dependence of elastic P- and S-wave velocities in porous Mt. Unzen dacite', *J. Volcanol. Geotherm. Res.*, vol. 153, no. 1, pp. 136–147, May 2006, doi: 10.1016/j.jvolgeores.2005.08.007.

[65] M. S. Jaya, S. A. Shapiro, L. H. Kristinsdóttir, D. Bruhn, H. Milsch, and E. Spangenberg, 'Temperature dependence of seismic properties in geothermal rocks at reservoir conditions', *Geothermics*, vol. 39, no. 1, pp. 115–123, Mar. 2010, doi: 10.1016/j.geothermics.2009.12.002.

[66] H. B. Motra and H. H. Stutz, 'Geomechanical Rock Properties Using Pressure and Temperature Dependence of Elastic P- and S-Wave Velocities', *Geotech. Geol. Eng.*, vol. 36, no. 6, pp. 3751–3766, Dec. 2018, doi: 10.1007/s10706-018-0569-9.

[67] L. Espinal, 'Porosity and Its Measurement', in *Characterization of Materials*, American Cancer Society, 2012, pp. 1–10.

[68] D. J. S. Roth, 'Review and statistical analysis of the ultrasonic velocity method for estimating the porosity fraction in polycrystalline materials', Jan. 1990. Accessed: Dec. 01, 2019. [Online]. Available: https://ntrs.nasa.gov/search.jsp?R=19900012086.

[69] K. Rasilainen *et al.*, *An interlaboratory comparison of methods for measuring rock matrix porosity*. VTT Technical Research Centre of Finland, 1996.

[70] Z. Fellah, M. Fellah, C. Depollier, E. Ogam, and F. Mitri, 'Ultrasound Measuring of Porosity in Porous Materials', 2018.

[71] T. Bourbie and B. Zinszner, 'Hydraulic and acoustic properties as a function of porosity in Fontainebleau Sandstone', *J. Geophys. Res. Solid Earth*, vol. 90, no. B13, pp. 11524–11532, 1985, doi: 10.1029/JB090iB13p11524.

[72] D. Han, A. Nur, and D. Morgan, 'Effects of porosity and clay content on wave velocities in sandstones', *GEOPHYSICS*, vol. 51, no. 11, pp. 2093–2107, Nov. 1986, doi: 10.1190/1.1442062.

[73] M. A. Biot, 'Theory of Propagation of Elastic Waves in a Fluid-Saturated Porous Solid. I. Low-Frequency Range', *J. Acoust. Soc. Am.*, vol. 28, no. 2, pp. 168–178, Mar. 1956, doi: 10.1121/1.1908239.

[74] M. A. Biot, 'Theory of Propagation of Elastic Waves in a Fluid-Saturated Porous Solid. II. Higher Frequency Range', *J. Acoust. Soc. Am.*, vol. 28, no. 2, pp. 179–191, Mar. 1956, doi: 10.1121/1.1908241.

[75] F. Gassmann, 'Elastic waves through a packing of spheres', *GEOPHYSICS*, vol. 16, no. 4, pp. 673–685, Oct. 1951, doi: 10.1190/1.1437718.

[76] X.-Q. Wang, A. Schubnel, J. Fortin, E. C. David, Y. Guéguen, and H.-K. Ge, 'High Vp/Vs ratio: Saturated cracks or anisotropy effects?', *Geophys. Res. Lett.*, vol. 39, no. 11, 2012, doi: 10.1029/2012GL051742.

[77] H. Kern, 'Measuring and Modeling of P- and S-Wave Velocities on Crustal Rocks: A Key for the Interpretation of Seismic Reflection and Refraction Data', *Int. J. Geophys. N. Y.*, vol. 2011, 2011, doi: http://dx.doi.org.libproxy.helsinki.fi/10.1155/2011/530728.

[78] E. I. Bajuk, M. P. Volarovich, K. Klíma, Z. Pros, and J. Vaněk, 'Velocity of longitudinal waves in eclogite and ultrabasic rocks under pressures to 4 kilobars', *Stud. Geophys. Geod.*, vol. 11, no. 3, pp. 271–280, Sep. 1967, doi: 10.1007/BF02585458.

[79] P. M. Benson, P. G. Meredith, E. S. Platzman, and R. E. White, 'Pore fabric shape anisotropy in porous sandstones and its relation to elastic wave velocity and permeability anisotropy under hydrostatic pressure', *Int. J. Rock Mech. Min. Sci.*, vol. 42, no. 7, pp. 890–899, Oct. 2005, doi: 10.1016/j.ijrmms.2005.05.003.

[80] S. Vinciguerra, C. Trovato, P. G. Meredith, P. M. Benson, C. Troise, and G. D. Natale, 'Understanding the Seismic Velocity Structure of Campi Flegrei Caldera (Italy): From the Laboratory to the Field Scale', *Pure Appl. Geophys.*, vol. 163, no. 10, pp. 2205–2221, Oct. 2006, doi: 10.1007/s00024-006-0118-y.

[81] Z. Pros, T. Lokajíček, and K. Klíma, 'Laboratory Approach to the Study of Elastic Anisotropy on Rock Samples', *Pure Appl. Geophys.*, vol. 151, no. 2, pp. 619–629, Mar. 1998, doi: 10.1007/s000240050133.

[82] R. Liebermann, 'Multi-anvil, high pressure apparatus: A half-century of development and progress', *High Press. Res.*, vol. 31, pp. 493–532, Dec. 2011, doi: 10.1080/08957959.2011.618698.

[83] T. Popp and K. Salzer, 'Anisotropy of seismic and mechanical properties of Opalinus clay during triaxial deformation in a multi-anvil apparatus', *Phys. Chem. Earth Parts ABC*, vol. 32, no. 8, pp. 879–888, Jan. 2007, doi: 10.1016/j.pce.2006.04.022.

[84] A. Aydin, 'Upgraded ISRM Suggested Method for Determining Sound Velocity by Ultrasonic Pulse Transmission Technique', *Rock Mech. Rock Eng.*, vol. 47, no. 1, pp. 255–259, Jan. 2014, doi: 10.1007/s00603-013-0454-z.

[85] A. McGarr and N. C. Gay, 'State of Stress in the Earth's Crust', *Annu. Rev. Earth Planet. Sci.*, vol. 6, no. 1, pp. 405–436, 1978, doi: 10.1146/annurev.ea.06.050178.002201.

[86] I. T. Kukkonen, V. Rath, L. Kivekäs, J. Šafanda, and V. Čermak, 'Geothermal studies of the Outokumpu Deep Drill Hole, Finland: Vertical variation in heat flow and palaeoclimatic implications', *Phys. Earth Planet. Inter.*, vol. 188, no. 1, pp. 9–25, Sep. 2011, doi: 10.1016/j.pepi.2011.06.002.

[87] K. Lambeck and A. Purcell, 'Glacial rebound and crustal stress in Finland', Posiva Oy, POSIVA--03-10, 2003. Accessed: Dec. 08, 2019. [Online]. Available: http://inis.iaea.org/Search/search.aspx?orig_q=RN:35052322.

[88] O. Stephansson, C. Ljunggren, and L. Jing, 'Stress measurements and tectonic implications for Fennoscandia', *Tectonophysics*, vol. 189, no. 1, pp. 317–322, Apr. 1991, doi: 10.1016/0040-1951(91)90504-L.

[89] S. Savchenko and F. Gorbatsevich, 'Estimation of the stressed state of the rock mass in the area of the Outokumpu deep drill hole (OKU), Finland', *Acta Geodyn. Geomater.*, vol. 9, pp. 31–42, Jan. 2012.

[90] I. Kukkonen and J. Šafanda, 'Palaeoclimate and structure: The most important factors controlling subsurface temperatures in crystalline rocks. A case history from Outokumpu, eastern Finland', *Geophys. J. Int.*, vol. 126, pp. 101–112, Apr. 2007, doi: 10.1111/j.1365-246X.1996.tb05270.x.

[91] R. H. Vernon, *A Practical Guide to Rock Microstructure*, 2nd ed. Cambridge: Cambridge University Press, 2018.

[92] K. Västi, 'Petrology of the Drill Hole r2500 at Outokumpu, Eastern Finland – the Deepest Drill Hole Ever Drilled in Finland', *Spec. Pap. Geol. Surv. Finl.*, vol. 2011, Jan. 2011.

[93] P. Hölttä and P. Karttunen, 'Metamorphism as a function of depth in metasedimentary rocks of the Outokumpu Deep Drill Hole', *Spec. Pap. Geol. Surv. Finl.*, vol. 2011, Jan. 2011.

[94] G. Simmons and H. Wang, *Single Crystal Elastic Constants and Calculated Aggregate Properties. A Handbook*, 2nd edition. Cambridge, Mass: The MIT Press, 1971.

[95] M. Lenka and D. Sarkar, 'Determination of metastable zone width, induction period and primary nucleation kinetics for cooling crystallization of l-asparaginenohydrate', *J. Cryst. Growth*, vol. 408, pp. 85–90, Dec. 2014, doi: 10.1016/j.jcrysgro.2014.09.027.

[96] A. Myerson, *Handbook of Industrial Crystallization*. Butterworth-Heinemann, 2002.

[97] C. J. Brown and X.-W. Ni, 'Determination of metastable zone width, mean particle size and detectable number density using video imaging in an oscillatory baffled crystallizer', *CrystEngComm*, vol. 14, no. 8, pp. 2944–2949, Mar. 2012, doi: 10.1039/C2CE06628A.

[98] J. W. Mullin, *Crystallization*. Oxford, UNITED KINGDOM: Elsevier Science & Technology, 2001.

[99] P. G. Debenedetti, *Metastable Liquids*. Princeton, N.J: Princeton University Press, 1996.

[100] P. Duchstein, P. Ectors, and D. Zahn, 'Advances in Inorganic Chemistry - Chapter 13 - Molecular simulations of crystal growth: From understanding to tailoring', in *Advances in Inorganic Chemistry*, vol. 73, R. van Eldik and R. Puchta, Eds. Academic Press, 2019, pp. 507–529.

[101] Y. Jian-min and Z. Huan-xiang, *Biophysics And Biochemistry Of Protein Aggregation: Experimental And Theoretical Studies On Folding, Misfolding, And Self-assembly Of Amyloidogenic Peptides*. World Scientific, 2017.

[102] M. Perez, M. Dumont, and D. Acevedo Reyes, 'Implementation of classical nucleation and growth theories for precipitation', May 2008.

[103] A. V. M. Weber, 'Nucleus formation in supersaturated systems', *Z Phys Chem*, vol. 119, p. 277, 1926.

[104] W. Lauterborn and T. Kurz, 'Physics of bubble oscillations', *Rep. Prog. Phys.*, vol. 73, no. 10, p. 106501, Sep. 2010, doi: 10.1088/0034-4885/73/10/106501.

[105] Lord Rayleigh O. M., F.R.S, 'VIII. On the pressure developed in a liquid during the collapse of a spherical cavity', *Lond. Edinb. Dublin Philos. Mag. J. Sci.*, vol. 34, no. 200, pp. 94–98, Aug. 1917, doi: 10.1080/14786440808635681.

[106] J. R. G. Sander, B. W. Zeiger, and K. S. Suslick, 'Sonocrystallization and sonofragmentation', *Ultrason. Sonochem.*, vol. 21, no. 6, pp. 1908–1915, Nov. 2014, doi: 10.1016/j.ultsonch.2014.02.005.

[107] J. Dodds *et al.*, 'The Effect of Ultrasound on Crystallisation-Precipitation Processes: Some Examples and a New Segregation Model', *Part. Part. Syst. Charact.*, vol. 24, no. 1, pp. 18–28, 2007, doi: 10.1002/ppsc.200601046.

[108] 'MIL-STD-1376B(SH), US Navy Military Standard for Piezoelectric Ceramics'. Feb. 24, 1995, Accessed: Jul. 12, 2019. [Online]. Available: http://everyspec.com/MIL-STD/MIL-STD-1300-1399/download.php?spec=MIL_STD_1376B.666.pdf.

[109] K. Nakamura, Ed., *Ultrasonic Transducers: Materials and Design for Sensors, Actuators and Medical Applications*, 1 edition. Cambridge, UK ; Philadelphia: Woodhead Publishing, 2012.

[110] T. Elbra, R. Karlqvist, I. Lassila, E. Hæggström, and L. J. Pesonen, 'Laboratory measurements of the seismic velocities and other petrophysical properties of the Outokumpu deep drill core samples, eastern Finland', *Geophys. J. Int.*, vol. 184, no. 1, pp. 405–415, 2011, doi: 10.1111/j.1365-246X.2010.04845.x.

[111] H. M. Alatalo, H. Hatakka, M. Louhi-Kultanen, J. Kohonen, and S.-P. Reinikainen, 'Closed-Loop Control of Reactive Crystallization. Part I: Supersaturation-Controlled Crystallization of L-Glutamic Acid', *Chem. Eng. Technol.*, vol. 33, no. 5, pp. 743–750, May 2010, doi: 10.1002/ceat.200900550.

[112] P. J. Heikkinen, E. A.-L. Koivisto, and I. Kukkonen, 'FIRE high resolution seismic survey in Outokumpu', *Outokumpu Deep Drill. Proj. - Second Internatinal Workshop Programme Ext. Abstr.*, pp. 17–20, 2007.

[113] K. Västi, 'M 52.5/4222/04/R2500. Syväkairausraportti (Geological log).', Geological Survey of Finland, 2005.

[114] H. Kern, T. I. Ivankina, A. N. Nikitin, T. Lokajíček, and Z. Pros, 'The effect of oriented microcracks and crystallographic and shape preferred orientation on bulk elastic anisotropy of a foliated biotite gneiss from Outokumpu', *Tectonophysics*, vol. 457, no. 3–4, pp. 143–149, Oct. 2008, doi: 10.1016/j.tecto.2008.06.015.

[115] A. Nur and G. Simmons, 'Stress-induced velocity anisotropy in rock: An experimental study', *J. Geophys. Res. 1896-1977*, vol. 74, no. 27, pp. 6667–6674, 1969, doi: 10.1029/JB074i027p06667.

[116] A. Nur and G. Simmons, 'The effect of saturation on velocity in low porosity rocks', *Earth Planet. Sci. Lett.*, vol. 7, no. 2, pp. 183–193, Nov. 1969, doi: 10.1016/0012-821X(69)90035-1.

[117] H. Kern, T. Popp, F. Gorbatsevich, A. Zharikov, K. V. Lobanov, and Yu. P. Smirnov, 'Pressure and temperature dependence of VP and VS in rocks from the superdeep well and from surface analogues at Kola and the nature of velocity anisotropy', *Tectonophysics*, vol. 338, no. 2, pp. 113–134, Aug. 2001, doi: 10.1016/S0040-1951(01)00128-7.

[118] R. Přikryl, K. Klíma, T. Lokajíček, and Z. Pros, 'Non-linearity in multidirectional P-wave velocity: confining pressure behaviour based on real 3D laboratory measurements, and its mathematical approximation', *Geol. Soc. Lond. Spec. Publ.*, vol. 240, no. 1, pp. 323–334, Jan. 2005, doi: 10.1144/GSL.SP.2005.240.01.23.

[119]   L. Nicoud, F. Licordari, and A. S. Myerson, 'Polymorph control in batch seeded crystallizers. A case study with paracetamol', *CrystEngComm*, vol. 21, no. 13, pp. 2105–2118, 2019, doi: 10.1039/C8CE01428K.

# APPENDIX A

Table 7. Relationships between elastic moduli in an isotropic material [27].

| | Compr. wave modulus $M$ | Young's modulus $E$ | Shear modulus $\mu$ | Lame constant $\lambda$ | Bulk modulus $k$ | Poisson's ratio $\nu$ |
|---|---|---|---|---|---|---|
| $E,\nu$ | $\dfrac{E\cdot(1-\nu)}{(1+\nu)\cdot(1-2\nu)}$ | | $\dfrac{E}{2\cdot(1+\nu)}$ | $\dfrac{E\cdot\nu}{(1+\nu)(1-2\nu)}$ | $\dfrac{E}{3\cdot(1-2\nu)}$ | |
| $E,\mu$ | $\dfrac{\mu\cdot(4\mu-E)}{3\mu-E}$ | | | $\mu\cdot\dfrac{E-2\mu}{3\mu-E}$ | $\dfrac{\mu\cdot E}{3\cdot(3\mu-E)}$ | $\dfrac{E-2\mu}{2\mu}$ |
| $E,k$ | $\dfrac{3k\cdot(3k+E)}{9k-E}$ | | $\dfrac{3kE}{9k-E}$ | $\dfrac{3k\cdot(3k-E)}{9k-E}$ | | $\dfrac{3k-E}{6k}$ |
| $k,\nu$ | $\dfrac{3k\cdot(1-\nu)}{1+\nu}$ | $3k\cdot(1-2\nu)$ | $\dfrac{3k(1-2\nu)}{2\cdot(1+\nu)}$ | $3\cdot\dfrac{k\cdot\nu}{1+\nu}$ | | |
| $k,\mu$ | $k+\dfrac{4\mu}{3}$ | $\dfrac{9k\cdot\mu}{3k+\mu}$ | | $k-\dfrac{2\mu}{3}$ | | $\dfrac{3k-2\mu}{2\cdot(3k+\mu)}$ |
| $k,\lambda$ | $3k-2\lambda$ | $9k\cdot\dfrac{k-\lambda}{3k-\lambda}$ | $\dfrac{3}{2}\cdot(k-\lambda)$ | | | $\dfrac{\lambda}{3k-\lambda}$ |
| $\mu,\lambda$ | $\lambda+2\mu$ | $\mu\cdot\dfrac{3\lambda+2\mu}{\lambda+\mu}$ | | | $\lambda+\dfrac{2}{3}\cdot\mu$ | $\dfrac{\lambda}{2\cdot(\lambda+\mu)}$ |
| $\mu,\nu$ | $2\mu\cdot\dfrac{1-\nu}{1-2\cdot\nu}$ | $2\mu\cdot(1+\nu)$ | | $\mu\cdot\dfrac{2\nu}{1-2\nu}$ | $\dfrac{2\mu}{3}\cdot\dfrac{1+\nu}{1-2\nu}$ | |
| $\lambda,\nu$ | $\lambda\cdot\dfrac{1-\nu}{\nu}$ | $\lambda\dfrac{(1+\nu)(1-2\nu)}{\nu}$ | $\lambda\cdot\dfrac{1-2\nu}{2\nu}$ | | $\lambda\cdot\dfrac{1+\nu}{3\nu}$ | |